nature water

Article

https://doi.org/10.1038/s44221-025-00404-z

Mineralization of captured perfluorooctanoic acid and perfluorooctane sulfonic acid at zero net cost using flash Joule heating

Received: 8 December 2023

Accepted: 6 February 2025

Phelecia Scotland[1,2], Kevin M. Wyss[2], Yi Cheng[2], Lucas Eddy[2,3,4], Jacob L. Beckham[2], Justin Sharp[2], Youngkun Chung[5,6,7,8], Chi Hun Choi[1,2], Tengda Si[2], Bo Wang[5,6], Juan A. Donoso[5,6], Bing Deng[2], Yu-Yi Shen[9], Sarah Grace Zetterholm[10], Christopher Griggs[10], Yimo Han[1], Mason Tomson[9], Michael S. Wong[1,2,5,9], Boris I. Yakobson[1,2], Yufeng Zhao[1,11] ✉ & James M. Tour[1,2,3,12] ✉

Per- and polyfluorinated alkyl substances (PFAS), including perfluorooctanoic acid (PFOA) and perfluorooctane sulfonic acid (PFOS), are persistent environmental contaminants that have infiltrated freshwater systems. Granular activated carbon (GAC) is widely used for PFAS removal but becomes secondary waste (PFAS-GAC). Current treatment methods are energy intensive and release hazardous fluorocarbons. This study demonstrates electrothermal mineralization of PFOA and PFOS-GAC via flash Joule heating, a scalable and efficient process. Heating PFAS-GAC with sodium or calcium salts converts PFAS into inert fluoride salts with >90% fluorine conversion and >99% PFOA and PFOS removal. Simultaneously, the spent carbon is upcycled into flash graphene, offsetting treatment costs by US\$60–100 per kg. This solvent- and catalyst-free method substantially reduces energy use, greenhouse gas emissions and secondary waste. A techno-economic assessment highlights its scalability and environmental benefits, offering a rapid (~1 s), cost-effective solution for PFAS remediation and upcycling of waste carbon into high-value products.

Per- and polyfluorinated alkyl substances (PFAS)[1], also commonly known as 'forever chemicals', refer to a group of synthetic compounds that have a combined market size of US\$28 billion in 2023[2]. There are over 9,000 types of PFAS, all of them anthropogenic[1]. PFAS has been widely used in fire-fighting foams, CO_2-based dry cleaning, non-stick cooking surfaces, food containers, personal care products and aqueous-film-forming foams, making them pervasive in human society[3,4]. Although they have many commercial applications, these once indispensable chemicals have recently been linked to several adverse health effects, including cancer, immune suppression and damage to the reproductive system, liver, kidney and thyroid[5,6]. Due to their chemical inertness, PFAS are not readily decomposed or expelled from the body[7]. Now these persistent, toxic compounds are ubiquitous in drinking water, soil and the blood of humans and animals[8,9], posing an immediate threat to both health[8,9] and the environment[10–13].

PFAS-contaminated water is a crucial source of exposure to the general population[13,14]. In response to these concerns, the US Environmental Protection Agency (EPA) recently lowered the maximum contaminant level in drinking water of specific PFAS, including perfluorooctanoic acid (PFOA) and perfluorooctane sulfonic acid (PFOS), each from 70 ng l^{-1} to 4 ng l^{-1} (refs. 15,16). Physiochemical adsorption has become a common strategy to collect PFAS from water streams and comply with these stringent limit. In this strategy, PFAS is adsorbed by granular activated carbon (GAC)[17,18] via hydrophobic interactions or by

A full list of affiliations appears at the end of the paper. ✉e-mail: yzhao@corban.edu; tour@rice.edu

anion exchange resins[19] through ionic interactions. The chain length and functional groups of the PFAS substantially influence the efficiency of these techniques[7].

While they are effective at removing PFAS, sorption methods generate secondary sorbent wastes containing concentrated PFAS. These PFAS-laden sorbent wastes are typically incinerated[7,19–21] at temperatures exceeding 1,000 °C. Sometimes, incomplete incineration can release PFAS and produce small, volatile organic fluorinated compounds (VOF) that are often more toxic than the original PFAS[21–23]. Additionally, reports indicate that some incineration plants are causing PFAS contamination in surrounding soil[24], well beyond expected background levels[12]. Higher concentrations of PFOA have been detected at incinerator sites compared to upwind areas[25]. Commercial-scale incineration of PFAS-contaminated sludges has also yielded PFAS-contaminated secondary ashes[26]. This incomplete understanding of incineration by-products is among the reasons the Department of Defense has proposed banning or restricting the incineration of PFAS[27]. Such legislation aims to prevent the release of PFAS emissions into the atmosphere and mitigate potential health and environmental risks associated with PFAS exposure. These concerns highlight the urgent need to modify current thermal treatment approaches for PFAS[28] and to develop alternative methods for their destruction[29,30].

Here we demonstrate an efficient and straightforward strategy for disposing of PFAS-laden GAC (PFOA/PFOS-GAC) using flash Joule heating (FJH) to mineralize the sorbed PFAS, resulting in a definitive end-point for the F atoms. FJH is a process by which current passes through a medium and rapidly heats the medium to high temperatures to induce a chemical reaction (Supplementary Fig. 1). This technique has found broad applications in waste management and recycling. For instance, it has been used in the upcycling of waste materials[31,32], regeneration of graphite in spent lithium-ion batteries[33], the remediation of heavy metals and polycyclic aromatic hydrocarbons in soil[34] and recently the remediation of PFAS in soil even up to kilogram scales.[35] The mechanism of FJH uses the target feedstock as the heating medium, making it a fast and efficient indirect heating technique. The local electric fields within the sample can be very high, polarizing the atoms rendering them open shell systems subject to rapid chemical rearrangements and hybridization changes[36].

We demonstrate that >90% of PFOA-GAC (>96%) and PFOS-GAC (~90%) can be degraded during FJH, forming inorganic salts with <0.01% of the initial PFAS remaining, respectively. This is accomplished by the ≤1-s FJH of the PFAS-GAC in the presence of NaOH or $Ca(OH)_2$, achieving temperatures >2,000 °C and mineralizing the organic F to NaF or CaF_2, respectively. Molecular dynamics investigations reveal that sodium and calcium might function as catalytic reagents that promote the breakage of the C−F bond. Furthermore, our results demonstrate that no VOF are formed at optimal reaction conditions and only trace amounts of short-chain PFAS remain after FJH in the presence of mineralizing reagents. The GAC is converted into crystalline flash graphene, a valuable co-product that can be sold to offset the cost of the decontamination process. A life-cycle assessment (LCA) shows that this process offers low energy consumption and produces minimal greenhouse gas while upcycling toxic and concentrated secondary waste streams into valuable graphene and inert inorganic salts. We anticipate these results to provide a foundational technique for the clean and efficient upcycling of spent sorbent materials, enabling the more effective treatment of PFAS-contaminated water.

Results and discussion

Direct conversion of PFAS-GAC into inorganic fluoride salts by FJH

PFOA and PFOS were chosen as representative PFAS types, given their prevalence as contaminants in water streams. Here we detail the remediation process of PFOA-GAC. A mixture of PFOA-GAC and NaOH (Methods and Supplementary Section 9 for more details) was packed into a quartz tube with double-O-ring seals on each end, as illustrated in Fig. 1a. The packed sample exhibited a typical resistance of 1.2 to 2.0 Ω, a suitable resistance for direct-current FJH[37]. Supplementary Fig. 2 displays an image of the PFOA-GAC sorbent, before grinding or the addition of mineralizing agents. Conventional FJH utilizes direct-current (d.c.) capacitor discharges in which the energy of the discharge is determined by the voltage of the flash and the capacitance of the capacitors used. Electronic switches can interrupt these discharges so that the discharge duration can be controlled on a timescale of milliseconds to a few seconds. This enables the energy and the duration of FJH to be highly tunable, facilitating reaction optimization. The reactants were then subjected to FJH at 110 V to 150 V for durations of either 0.50 s or 1.00 s. These reactions resulted in a high current (Fig. 1b) and a rapid temperature increase up to >3,000 °C (Fig. 1c), which decays over the course of 2 to 3 s.

The high temperatures achieved by the rapid resistive heating resulted in the reaction of PFOA with NaOH, forming NaF through the strong bond association of the fluoride anion to the sodium cation (Supplementary Fig. 3). NaOH was selected as the mineralizing reagent due to the higher solubility of NaF in water, facilitating easier and more accurate quantification of the mineralization efficiency. Whereas $Ca(OH)_2$ might be more optimal for industrial use because the most common mineralized form of fluoride is the calcium salt CaF_2, the solubility advantage of NaF makes NaOH a better choice for our purposes.

The resulting products were analysed using ion chromatography (IC) to quantify the degree of mineralization and liquid chromatography-mass spectrometry (LCMS) to measure the PFAS removal efficiencies. The best results for the mineralization of PFOA- and PFOS-laden GAC were ~96% and ~90%, respectively, with PFAS removal efficiencies >99.9% (Fig. 1d). Figure 2 provides a more detailed analysis of the reaction of PFOA-GAC. (0.927 ± 0.063) wt% or ~96% of organic F in PFOA was converted to inorganic fluoride at 130 V for 1.00 s when 1.2 mole equivalent (eq) of NaOH was used per mole of fluoride in the starting stock (Fig. 2a). When the control PFOA-GAC (without sodium or calcium) was FJH at 130 V for 1.00 s, only (0.370 ± 0.138) wt% or ~38% of the total F was detected in the form of inorganic fluoride by IC analysis (Supplementary Table 1 and Extended Data Fig. 1a,b). This underscores the role of NaOH in enhancing the conversion efficiency of organic F to inorganic fluoride during FJH treatment, as demonstrated by the substantially higher mineralization rate observed in the presence of sodium ions. This provides a definitive end-point for the F atoms. Approximately 90% of F in PFOS was recovered as inorganic fluoride when FJH at 130 V for 2.00 s and a higher loading of initial sodium (Methods).

The sample mass, capacitance and voltage discharged through the sample directly determine the thermal energy generated and the highest temperature achieved. Supplementary Table 2 shows the results of the Welch two-sample *t*-test analysis to gauge the significance of using different voltage and reaction times in our experiments. The comparison of inorganic fluoride yield under various conditions reveals a substantial trend: higher voltages and longer reaction times generally enhance recovery. However, there is a threshold where further voltage increases do not substantially improve yield, exemplified by the little difference between 130 V and 150 V for 1.00 s. Operating at 150 V poses practical challenges such as tube cracking, sample loss and side reactions. Comparing 110 V for 1.00 s to 130 V for 0.50 s shows comparable yields, suggesting that extending reaction time at lower voltage compensates for shorter, higher-voltage reactions. This underscores the importance of balancing voltage and duration in flash reactions, where adjusting duration can optimize yield without raising voltage, providing flexibility and kinetic control over fluoride mineralization. We then studied the localization of soluble inorganic fluoride, such as NaF, within the reaction vessel. Figure 2b,c shows the recovery location of these salts within the reactor, as quantified by ion chromatography. The inorganic salts were found largely mixed with the solid powder flash

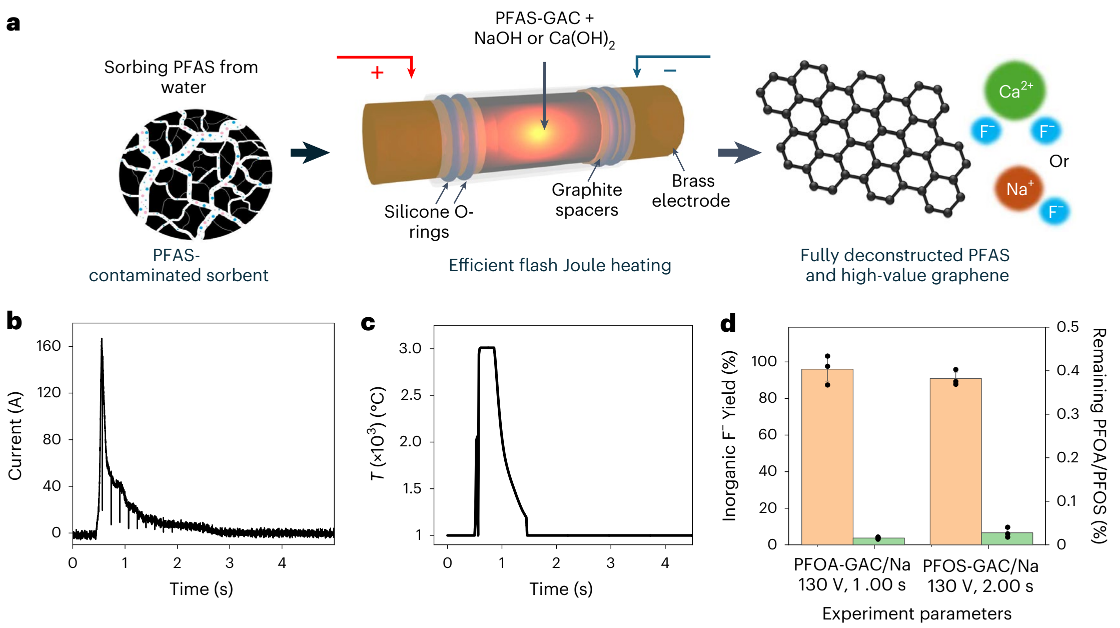

Fig. 1 | Scheme, current and temperature of the FJH study. a, Schematic of the experimental set-up and process. **b**,**c**, The current profile of a typical 150 V (59 mF, 1.00 s FJH experiment (**b**) and the temperature profile of the FJH over the course of the reaction (**c**). This temperature was measured using a Micro-Epsilon CTRM1H1SF100-C3 pyrometer with 1-ms resolution and a 1,000 °C–3,000 °C temperature range. **d**, Summary of mineralization and degradation of PFOA- and PFOS-laden GAC; >90% of inorganic F can be recovered using FJH. In **d** the data are presented as the mean ± standard deviation (s.d.) of the IC and LCMS results from three parallel experiments ($n = 3$).

graphene (FG) product and deposited onto the graphite electrodes and with small amounts adhered to the inner walls of the quartz tube.

High-resolution X-ray photoelectron spectroscopy (XPS) in Fig. 2d compared the PFOA-GAC with the products from the FJH reaction at 150 V and 1.00 s. The F 1*s* peak of PFOA-GAC appears at a higher binding energy (688.9 eV) compared to that of the flashed product (684.5 eV). The corresponding F 1*s* peak of the product can be deconvoluted to a NaF peak at 684.5 eV and a second peak at 686.0 eV, indicating sodium fluorosilicate $Na_2(SiF_6)$. The $Na_2(SiF_6)$ is present in small amounts due to the reaction with the quartz tube. $Na_2(SiF_6)$ is water soluble, and the resultant anion can further dissociate into water to give fluoride ions (Supplementary Fig. 4)[38]. Thus, the fluoride formed as $Na_2(SiF_6)$ is detected in the IC data. Fluorine-19 nuclear magnetic resonance spectroscopy (^{19}F NMR) also shows the disappearance of the PFOA peaks and the formation of a distinct inorganic fluoride peak (Fig. 2e).

To determine if any PFOA remained after the FJH reactions, the flash graphene and reactor components were washed (Methods) and the filtrates were analysed using LCMS (Fig. 2f). The LCMS and IC calibration curves are shown in Supplementary Fig. 5. On average, <0.01% of PFOA remains when FJH reaction conditions are at 150 V and 1.00 s. However, we performed the following F mass balance using experiments conducted at 130 V and 1.00 s, because these parameters gave us the highest mineralization ratio. LCMS determined that ($0.000151 \pm 1.999 \times 10^{-5}$) wt% of F from PFOA remained after the reaction. This accounts for 0.0156% of the starting fluorine. Thus the removal efficiency of this process is ~99.98% for PFOA. The removal efficiency was calculated using equation (1), where C_0 and C_F are the initial and final concentrations, respectively.

$$\%\text{Removal} = \frac{C_0 - C_F}{C_0} \times 100 \qquad (1)$$

Further, LCMS determined that ($0.001173 \pm 1.62441 \times 10^{-4}$) wt% of F from PFOA remained in the control samples when no sodium was used. This accounts for 0.122% of the starting fluorine. Hence, the removal efficiency was lowered to ~99.88% for PFOA (Extended Data Fig. 1c and Supplementary Table 3).

Short-chain perfluorocarboxylic acid degradation products (C_4 to C_7) were detected using LCMS. The total concentration of F from the C_4–C_7 degradation products was ($0.0001031 \pm 9.39348 \times 10^{-6}$) wt%, representing 0.0107% of the initial F content. In the absence of sodium, the average remaining organic F (C_4 to C_7) was ($0.00029973 \pm 3.18955 \times 10^{-5}$) wt%, constituting 0.0311% of the initial F (Extended Data Fig. 1d). These findings indicate that the presence of sodium reduces the occurrence of short-chain PFCAs. Further, residual short-chain PFCAs could potentially be mineralized more effectively under higher voltages, prolonged reaction times or increased concentrations of initial sodium ions.

Gas chromatography-mass spectrometry (GC-MS) was used to ascertain whether VOF were being generated. Using a partially sealed set-up described in Extended Data Fig. 2a, the off gas from the reaction was captured and tested. GC-MS revealed a discernible trend: an increase in the stoichiometric ratio of NaOH corresponded to a decrease in the presence of evolved VOF (Fig. 2g). In the chromatogram, the peak between 2.15 to 2.22 min corresponds to air. The peaks labelled 1, 2 and 3 correspond to gases released during the reactions and were identified as perfluoropentene, perfluorohexene and perfluoroheptene, respectively. The mass spectra of these compounds are shown in Extended Data Fig. 2b–d. Importantly, the addition of 1.2 mol eq of NaOH per F atom in a PFOA-GAC mixture resulted in a 99.81% reduction of VOF at 130 V for 1.00 s, as illustrated in Fig. 2h and Supplementary Table 4. This result shows that excess mineralizing reagents can mitigate the formation of VOF in the degradation of PFOA-GAC. Supplementary Figs. 6–9 and Supplementary Table 5 provide additional support for the reduction of VOF in this set-up.

During FJH, GAC was transformed into highly crystalline turbostratic flash graphene. Figure 2i illustrates the graphene yield for a representative set of samples obtained during the experimental process, affording >95% yield at 150 V for a 1.00 s flash. Additional spectroscopic microscopic and reaction details regarding the produced graphene can be found in Extended Data Fig. 3 and Supplementary Figs. 10–19.

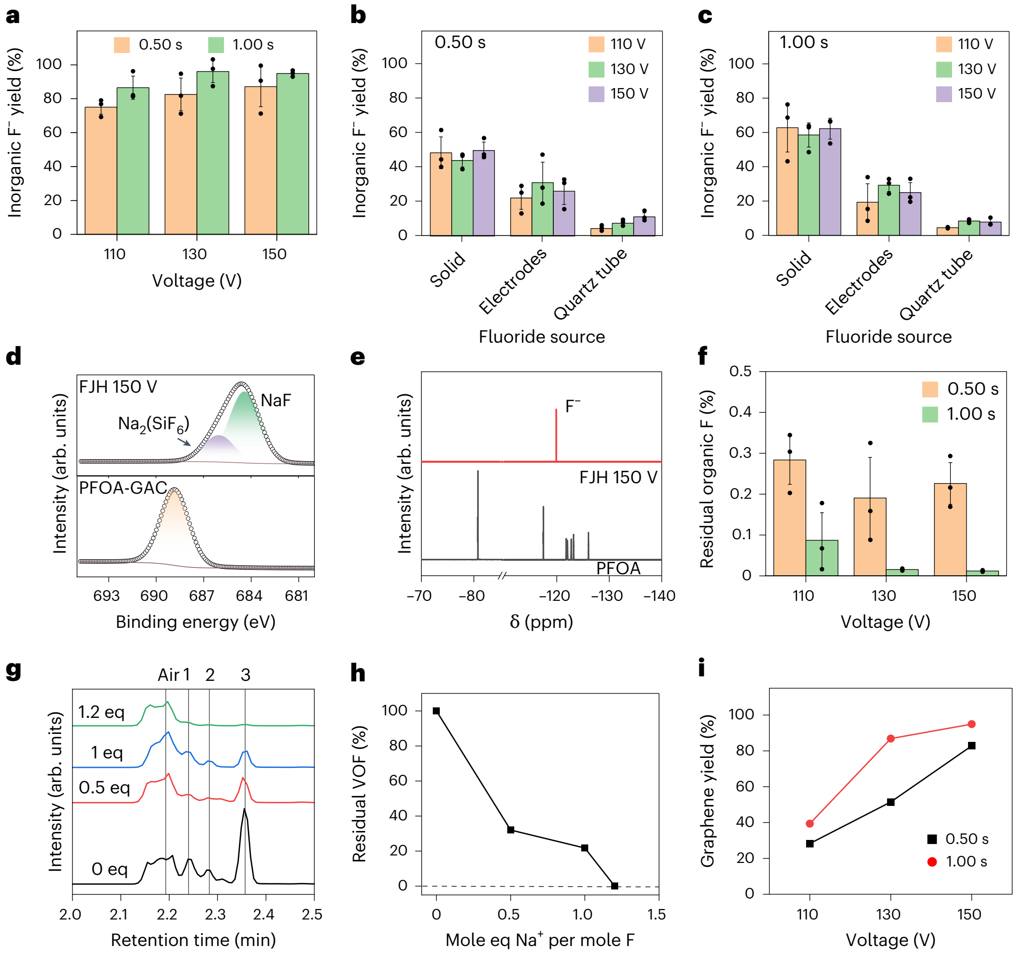

Fig. 2 | Quantification and analysis of the mineralization process. a, Inorganic fluoride yield from FJH reaction of PFOA-GAC with 1.2 molar eq of sodium per mole of fluoride in PFOA (*n* = 3). **b**,**c**, The average mass yield distribution of the fluoride recovered from various parts of the reactor for different reaction conditions at 0.50 (**b**) and 1.00 s (**c**) flash durations, respectively (*n* = 3). **d**, High-resolution F 1*s* spectrum of the PFOA-GAC and fluoride salt/flash graphene product. **e**, ^{19}F NMR spectra of PFOA-GAC and flash graphene product. **f**, LCMS analysis of residual organic F recovered from the rinsed product (*n* = 3). **g**, GC-MS analysis of VOF produced during the reaction using varying mole eq ratios of sodium per mole of fluoride in PFOA (*n* = 1). Peaks 1, 2 and 3 correspond to the VOF evolved during the reactions and were identified as perfluoropentene, perfluorohexene and perfluoroheptene, respectively. **h**, Remaining VOF with increasing molar eq of sodium per mole of fluoride (*n* = 1 experiment per reaction condition). **i**, Graphene yield for the FJH samples, showing representative graphene samples from the experimental process (*n* = 1 sample per reaction condition). All error bars represent standard deviation. In **a**–**c** and **f**, the data are presented as the mean ± s.d. of the results from three parallel experiments (*n* = 3).

We achieved the recovery of ~96% of the initial F content under the reaction conditions of 130 V for 1.00 s (*n* = 3). The missing F from the total mass balance was then investigated. The reaction tube post-FJH shows substantial blackening, especially near the middle section, furthest from the heat-sinking electrodes, where the reaction becomes hottest (Supplementary Figs. 20 and 21). After washing the tube and drying, Raman spectroscopy (Supplementary Fig. 22 and Supplementary Table 6) and XPS (Supplementary Figs. 23 and 24 and Supplementary Table 7) reveal peaks indicative of insoluble sodium fluorosilicate, possibly $NaSiF_3O$[39]. The atomic percentage after rinsing ranges from 2.68% to 3.63% on the surface of the tube (Supplementary Table 7). However, because XPS is a surface analytical method, it is difficult to quantitate this additional deposit of F into a complete mass balance, but it is suggestive that the residual trace fluoride is not volatilized through the double-O-ring seals but reactive with the FJH vessel[29]. As shown in Supplementary Fig. 25, voltage plays a critical role in this process. Although the PFOA removal efficiency for GAC/PFOA (without sodium), FJH at 130 V and 1.00 s was 99.88%, only 38.49% of total F could be accounted for using our current analytical techniques. A stark difference when compared to the sample FJH with excess sodium. Additional characterization for the remediation of PFOS-GAC is shown in Extended Data Fig. 4.

Other PFAS sorbents and mineralizing reagents

Other ionic salts can be used to promote the mineralization of fluorine. Extended Data Fig. 5 shows the efficacy of $Ca(OH)_2$ as a mineralizing reagent. In keeping with the methodology employed for reactions using NaOH, PFOA-GAC was mixed with excess $Ca(OH)_2$ (Methods) and subjected to FJH. The reaction at 150 V for 0.50 s resulted in 94% of the fluoride being converted into CaF_2. Due to the low solubility of CaF_2, the actual mineralization ratio might be slightly underreported. Graphene is also produced in high yield (Extended Data Fig. 5d–g). The inner surface of the reaction tube was analysed using XPS (Supplementary Fig. 26) after rinsing with 0.1 M of H_2SO_4 and drying. Up to 1.62% of surface fluoride can remain on the blackened area of the post-reaction tube after washing (Supplementary Table 8).

Alternative sorbents, such as anion exchange resins, offer an effective means of PFAS removal from water. One such example is Purofine PFA694 resin, consisting of polystyrene beads with an amine-functional group. FJH of this PFOA resin is described in Extended Data Fig. 6.

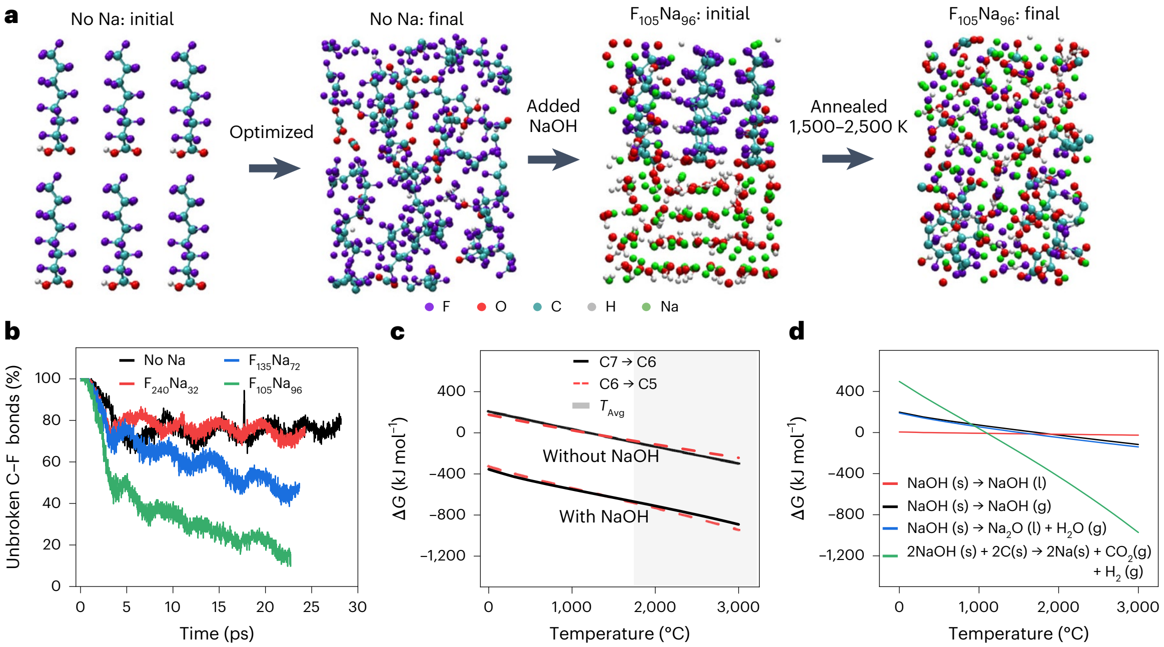

Fig. 3 | Simulations of PFOA reacting with NaOH at high temperatures. **a**, Schematic of molecular dynamics simulation of optimized PFOA with the highest loading of NaOH ($F_{105}Na_{96}$), annealed between 1,500 and 2,500 K. **b**, Number of unbroken C–F bonds calculated based on **a**. **c**,**d**, Thermodynamic analysis using the HSC chemistry package. **c**, The favourability of the reaction between fluorocarbons in the presence or absence of NaOH. **d**, The change in the Gibbs free energy suggests the most favourable reaction pathways for the NaOH mineralizing reagent during heating.

We also demonstrate that even polytetrafluoroethylene (PTFE, commonly known as Teflon), one of the most recalcitrant types of PFAS with a melting point of ~327 °C (ref. 40), undergoes mineralization. Although Teflon is not water soluble and therefore not a typical water contaminant, the successful mineralization of this type of PFAS using FJH highlights the versatility of our technique (Supplementary Fig. 27).

Molecular dynamics simulations

Optimized structures of PFOA and varying concentrations of NaOH were computationally heated at the temperature oscillating between 1,500 and 2,500 K for 30 ps (Fig. 3a). Because the reaction leads to the cleavage of the C–F bonds in the PFAS, the number of C–F bonds in the system was used as a descriptor (Fig. 3b). The results of these simulations interestingly revealed a catalytic role for the mineralization salts during an FJH reaction. In the absence of sodium salts, ~80% of the C–F bonds remained unbroken after annealing. For F to Na ratios of $F_{240}Na_{32}$, $F_{135}Na_{72}$ and $F_{105}Na_{96}$ (in order of lowest to highest loading of Na), the amount of unbroken C–F bonds was 78%, 48% and 15%, respectively. These reactions show that the ratio of unbroken bonds is substantially reduced with the addition of higher concentrations of sodium salts when annealed under similar conditions. Thus, sodium ions themselves promote the breakage of the C–F bond and enhance the rate of mineralization. Similar catalytic properties probably exist for other alkali metals and alkaline earth metals. Supplementary Fig. 28 shows the simulated and optimized structures for the lowest and intermediate loading of sodium salts.

Whereas a precise mechanism for PFOA degradation via FJH remains elusive, insights can be obtained from these molecular dynamics (MD) simulations and the observable reaction products. Extended Data Figs. 7 and 8a show the MD simulated intermediate steps for two distinct reaction pathways between NaOH and PFOA. The first four steps ((i)–(iv); Extended Data Figs. 7 and 8a) in the reaction pathways are the same, signifying that the initiation of the reduction process is similar. However, the bonding environments of the intermediary species diverge from steps ((v)–(viii); Extended Data Figs. 7 and 8a) onwards. Energetic calculations were conducted for each step in the reaction pathway in Extended Data Fig. 8b. Pathway 1 had lower energy for steps (v)–(viii), probably due to a more favourable bonding environment in the intermediate species.

In both pathways, the reaction was driven by the reduction of F by sodium ions. Due to the high electronegativity of F atoms, the C–F covalent bonds are highly frustrated, and the replacement of F with OH or the removal of F through forming C = C double bonds is thermodynamically favourable. The activation energy required to displace F atoms and form more thermodynamically favourable products is probably lowered in the presence of sodium salts.

Thermodynamic analysis

Further theoretical analysis was conducted by calculating the change in the Gibbs free energy of the degradation steps after the decarboxylation of PFOA. In the absence of NaOH, shorter-chain VOF can be formed, such as C_7F_{14}, C_6F_{12} and C_5F_{10}. It is known that PFOA tends to first decarboxylate upon heating, followed by subsequent reduction of its radical intermediary. C_7F_{15} (ref. 23). The loss of a F atom followed by rearrangement of the C–C bond to a C = C bond would produce C_7F_{14}, and the subsequent loss of -CF_2 and -C_2F_4 would produce C_6F_{12} and C_5F_{10}, respectively. Figure 3c shows that these reactions are highly exothermic in the presence of NaOH due to the formation of NaF. This principle extends to $Ca(OH)_2$, which forms the highly thermodynamically stable CaF_2 upon mineralization (Extended Data Fig. 5c).

Figure 3d shows the possible state of the NaOH during the reaction, and the Gibbs free energy of the reaction is illustrated in Supplementary Figs. 29 and 30. In this work, temperatures >2,500 °C can be achieved and reaction durations are on the millisecond to seconds timescale. As a result, the FJH process experiences rapid heating and cooling rates[37,41]. Given that the boiling points of most of the reactants are below this temperature, it is likely that the reactants vaporize or sublime, considering the reaction timescale. The gaseous products then mix to bring the mineralizing reagent into closer contact with the PFOA and react to form inorganic fluoride compounds that deposit and are further analysed and quantified. Extended Data Fig. 9 summarizes these species and their physical state during the experiment.

https://doi.org/10.1038/s44221-025-00404-z

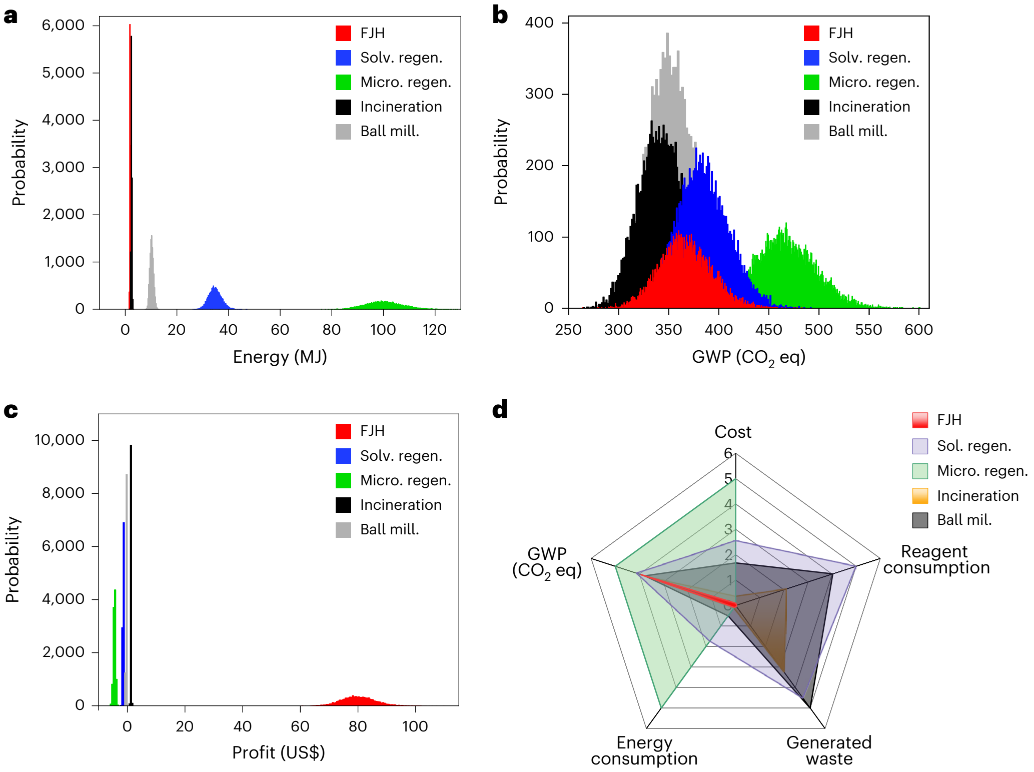

Fig. 4 | Comparative LCA and TEA of FJH as compared to other PFAS-GAC remediation methods. a, Process energy demand in MJ per kg of treated GAC. **b**, The global warming potential (GWP) in kg of CO_2 emitted per kg of treated GAC. **c**, The profit margin of each GAC remediation method studied. **d**, A five-point radar plot illustrating the cumulative assessment of key environmental impacts and costs for each process studied. Variables are normalized on a scale from 0 to 5, where 5 represents the highest normalized value for each variable within a given process. Solv. regen., solvent regeneration; Micro. regen., microwave regeneration; Ball mill., ball milling.

The green line in Fig. 3d represents the carbothermal reduction of NaOH during FJH conditions, forming sodium metal (Na(0)) when $T > 1{,}140$ °C. This is an impetus for moving to use calcium salts such as $Ca(OH)_2$ or CaO when scaling up to minimize the accumulation of the more reactive Na(0).

LCA and techno-economic assessment

Due to the prevalent use of GAC to remove PFAS from wastewater, copious amounts of this contaminated carbon are generated, so a variety of disposal pathways are currently being explored. To compare this FJH mineralization process to these other PFAS-GAC remediation methods, comparative LCAs and techno-economic assessments (TEAs) were conducted. LCAs and TEAs are analytical methodologies used to examine the environmental impact and associated costs of a product or process throughout its life cycle, from raw material extraction to waste disposal[42–44].

Here five different PFAS-GAC disposal scenarios are compared: direct incineration/thermal heating[28], ball milling assisted mineralization[45], regeneration of GAC by microwave heating[17], solvent extraction[46] and mineralization by FJH. Regeneration processes tend to focus on reusing the GAC and often operate at lower temperatures to avoid affecting the GAC[17,46]. Although we primarily used NaOH as the mineralizing reagent in FJH experiments to facilitate the quantification of mineralized fluoride, we posit that in a scaled-up process, a calcium-based mineralizing reagent would be used due to these reagents being more cost effective and without the generation of the more reactive sodium metal through carbothermic reduction during FJH. We have demonstrated that $Ca(OH)_2$ can be used as an effective mineralizing agent as shown in Extended Data Fig. 5. Furthermore, the inert and non-toxic by-product, CaF_2, is more attractive because it is a natural mineralized form of fluoride in the environment; hence, the LCA and TEA were performed with $Ca(OH)_2$ (ref. 47).

Figure 4a shows the process energy demand for each method in MJ. The energy consumption of FJH to incineration is comparable. However, ball milling, solvent regeneration and microwave processes consume 5, 18 and 52 times more energy than FJH, respectively. Figure 4b shows the greenhouse gas emissions for each process in the form of global warming potential or the kg of CO_2 released to produce 1 kg of treated GAC for each method. CO_2 emissions of FJH, incineration and ball milling are comparable. However, solvent regeneration and microwave processes release 5, 27 percent more CO_2 than FJH, respectively. Figure 4c shows the TEA results for the profit of each process in US$. The TEA accounts for known scaled processes where solvents can be recycled with ~95% efficiency to reduce costs. The TEA does not account for the cost of treatment or disposal of additional waste streams produced by the process, which can further increase treatment costs. A plotted histogram of the costs is shown in Supplementary Fig. 31. Figure 4d depicts a radar plot which collectively assesses the previously addressed variables and other factors including the amount of reagents used and generated waste streams. Considering the typical PFAS content on GAC is ≤1 wt %, the amount of CaF_2 generated in the flash graphene product is minimal. However, this LCA accounts for the worst-case scenario of PFAS content in GAC, which can be as high as 10 wt%. In most cases, the non-toxic CaF_2 would not have to be removed, especially if the product flash graphene is slated for use in concrete and asphalt, which is the largest potential market for this material[47]. The full LCA breakdown is found in Supplementary Section 8.

The process cost is largely dependent on the electrical consumption used in each method. Notably, personnel and transportation costs were excluded from this analysis due to insufficient data in the literature. With FJH mineralization of the starting material, GAC, valuable graphene can be produced, which is typically listed between US$60 and $100 per kg (ref. 48). Taken together, these assessments underscore the prospect of FJH for the mineralization of PFAS-laden sorbents. Translating findings from controlled environments to real-world scenarios can present challenges. However, it's crucial to note that even at the lab scale, LCA and TEA can provide valuable insight into the environmental impacts and cost of processes and products. These insights can inform decisionmaking, guide improvements and pave the way for more sustainable practices as technologies scale up. Whereas there might be discrepancies between lab-scale and real-world conditions, the exercise itself fosters awareness and drives innovation towards more environmentally friendly solutions.

High-frequency induction heating[29] and plasma heating[30] are additional examples of thermal treatment methods and have recently been utilized in the treatment of PFAS-GAC at the laboratory scale. A brief comparison to FJH is demonstrated in Supplementary Table 9. Future directions include scaling up these reactions for practical application. A 3 g PFOA-GAC demonstration was conducted, and the results are detailed in Extended Data Fig. 10 and Supplementary Fig. 32, highlighting the potential for larger-scale treatments.

Conclusion

This work demonstrates that the FJH process can rapidly degrade PFAS compounds, specifically PFOA, PFOS and even PTFE in the presence of mineralizing agents while producing little or no harmful shorter-chain PFAS, VOF or hydrogen fluoride. Though demonstrated here for PFOA, the most common type of PFAS found in water, the FJH reaction temperatures of >2,000 °C will probably cause decomposition and mineralization of most PFAS types when in the presence of sodium or calcium salts. Valuable graphene is produced as a product of this reaction, the sale of which can result in superior economic viability compared to other disposal methods that do not produce high-value co-products. Instead of generating graphene, small modifications of the FJH process can alternatively afford carbon nanotubes, nanodiamonds or amorphous carbon, expanding the scope of the final carbon products[49].

Methods

Sample preparation

PFOA-GAC in the amount of 0.40 g (39.48 mg of PFOA) was mixed with 69 mg of NaOH (1.2 mole eq of sodium per mole of F in PFOA). The sample was ground with a mortar and pestle to ensure that the NaOH was in close contact with the PFOA. Then 0.20 g of the mixture was mixed with 1.00 g of neat GAC and ground using a mortar and pestle providing a calculated starting concentration of ~14.03 mg PFOA g^{-1} sorbent (9.65 mg F g^{-1} sorbent or 0.965 wt%). To verify this, we used combustion ion chromatography (CIC) to determine the total F content in solid or liquid samples. The average F concentration of the starting feedstock was (0.951 ± 0.022) wt% ($n = 3$ and $R^2 = 0.9980$). The calculated value of 0.965 wt% is within this range so we used the calculated value to determine the removal and mineralization efficiency (Supplementary Table 10).

Stock material in the amount of 0.10 g was subjected to FJH using a double-O-ring-sealed system (Fig. 1a). The quartz tubes are prone to being shattered due to the pressure difference inside and outside of the tube. Thus a spring wrapped outside the tube reduced the likelihood of tube shatter. The typical resistance across the sample in the quartz tube is 1.2 to 2.0 Ω. The current discharge is an unmodulated d.c. discharge with a capacitance of ~59 mF, with the initial voltage and pulse time ranging from 110 to 150 V and 0.50 to 1.00 s. To ensure thorough washing and extraction, the samples were rinsed with excess high-performance liquid chromatography grade water (20 to 50 ml) after FJH and subjected to agitation by shaking for 24 h. The samples are then sonicated for 10–15 min to release any F by-products that might remain on the flash graphene (FG) or on the reactor components.

PFOA-GAC in the amount of 0.40 g (39.48 mg PFOA) was mixed with 53 mg of $Ca(OH)_2$ (0.5 calcium ions for every fluoride atom). A 0.1-g amount of this mixture was mixed with 0.80 g of neat GAC. A 0.10-g amount of this feedstock should yield a theoretical amount of 0.633 mg of inorganic F from CaF_2. The sample was FJH at 110 to 150 V, respectively, with a duration of 0.50 s and a discharging capacity of 59 mF. A 0.1-M amount of H_2SO_4 was used to rinse the post-reaction samples to leach the CaF_2.

GAC in the amount of 1.55 g (F400) was added to 20 ml of PFOS solution (498.4 ± 5.35 pm). The filtrate had a PFOS concentration of 4 ppm (To bypass the need for solid-state dilution and minimize tube breakage, a lower concentration of PFOS was adsorbed onto GAC). The adsorbed F from PFOS concentration was calculated to be 5.89 mg. A 0.5-g amount of PFOS-GAC (~3.87 mg F g^{-1}) was mixed with 10.1 mg of NaOH (2.5 molar eq of sodium), this high loading of NaOH was to ensure that the PFOS-GAC was properly mixed and coated with NaOH so that the sodium ions could be in close contact with the PFOS. The mixture had a calculated concentration of 3.79 mg F g^{-1} or 0.379 wt%. CIC was used to further analyse the starting F concentration and 0.387 ± 0.0216 wt% for $n = 3$. Subsequently, 0.1 g (~3.79 mg F g^{-1} or 0.379 wt%) of this sample underwent FJH at 130 V for 2.00 s.

Because PTFE is not soluble in water, 10 mg of PTFE was mixed with 32.5 mg of NaOH (2 mole equiv of sodium per mole of F in PTFE). The mixture was ground using a mortar and pestle. Approximately five drops of water were added followed by 0.6 g of GAC (F400). The water was added to help the PTFE and NaOH mixture coat the GAC. After further grinding, the mixture was dried in an oven at ~400 F for 30 min. A 0.6-g amount of stock material was FJH twice at 130 V for 2.00 s. The current ranged between 214 and 322 amps and 393 and 438 amps on the first and second flash, respectively. The reactions had a near complete voltage discharge on the second flash. The calculated concentration of F in 0.6 g of sample was 0.709 mg F.

Different PFAS compounds might require varying concentrations of mineralizing agents to achieve near complete destruction. The use of excess reagents, coupled with optimal reaction conditions, can promote high mineralization yields and enhance PFAS removal efficiency. However, when the initial PFAS loading is low, it might be necessary to add additional mineralizing reagent. This ensures that the PFAS-GAC is uniformly mixed because the mineralizing agent is not applied directly to the PFAS but rather to the PFAS-loaded GAC. By ensuring a uniform distribution, the effectiveness of the mineralization process is maintained, even at low PFAS concentrations.

Implementation of this FJH PFAS destruction method requires scaling up this technique. Recently, two separate kg-scale FJH methods have been demonstrated. One consists of using an automated system to rapidly flash Joule heat ~6 g batches of feedstock to obtain 1 kg of product[50]. The other consists of performing a long-duration FJH reaction on a single kg of sample[35]. Either of these methods could be implemented to remediate PFAS from GAC and convert the GAC to graphene at kg scales and beyond. For scaling up or on an industrial scale, we recommend the use of concrete blocks with holes drilled in the centre as a robust, chemically inert sample holder for the remediation of PFAS. This could minimize the side reactions we observed when using quartz as the reactor.

Characterization

The filtrates from the washing of the FJH products were analysed for inorganic fluoride anions using ion chromatography on a Thermo Scientific Dionex Aquion. Chromatographic separation was achieved using the Dionex IonPac AS23 IC Column 4 × 250 mm. The Mobile phase consists of 4.5 mM Na_2CO_3 and 0.8 mM $NaHCO_3$. The flow rate was 1 ml min^{-1} and the column temperature was 30 °C. The resultant peaks were fitted between 4 and 5 min. We also employed an alternative IC instrument when the Thermo Scientific Dionex Aquion was unavailable. The Metrohm 930 Compact IC Flex with column 4 × 250 mm.

The eluent consisted of 3.2 mmol l^{-1} Na_2CO_3 and 1.0 mmol l^{-1} $NaHCO_3$, column temperature 25 °C, flow rate 0.700 ml min^{-1}, column pressure 11.83 MPa. The conductivity should be below 1.2 μS cm^{-1} before the run. The fluoride peak was set at 6.10 min and the concentration was taken based on the area under the peak within a 5% window.

Two LCMS instruments were used. The first was an Agilent 1290 Infinity Binary Pump LC coupled to an Agilent 6495 C triple quadrupole MS/MS with Jet Streaming Technology and electrospray ionization (ESI). Chromatographic separation was performed using an Agilent Zorbax Eclipse Plus C18 column (2.1 × 100 mm, 1.8 μm). An Agilent Infinity Lab PFC Delay Column (4.6 × 30 mm) was used to delay any possible PFAS that is inherently in the system or mobile phases. The aqueous phase consisted of 2 mM ammonium acetate with 5% acetonitrile in MS-grade water (Solvent A) and 100% MS-grade acetonitrile (solvent B). Chromatographic separation required a gradient elution with a flow rate of 0.35 ml min^{-1}. The analytical column was maintained at 40 °C throughout the run. The injection volume was 5 μl for this analysis. Data acquisition was performed in dynamic multiple reaction monitoring mode using negative-mode ESI.

The second LCMS instrument was the Agilent 1290 Infinity Binary Pump LC coupled to an Agilent 6470B triple quadrupole MS/MS through an Agilent Jet Spray ESI in negative ionization mode. Chromatographic separation was performed using an Agilent Zorbax Eclipse Plus C18 column (2.1 × 100 mm, 1.8 μm). An Agilent Infinity Lab PFC Delay Column (4.6 × 30 mm) was used to delay any possible PFAS that is inherently in the system or mobile phases. The injection volume of samples was 40 μl during the analysis. The aqueous phase consisted of 20 mM ammonium acetate in MS-grade water (solvent A) and 100% MS-grade methanol (MeOH) (solvent B). Chromatographic separation required a gradient elution with a flow rate of 0.4 mL min^{-1}. The composition of mobile phase was ramped from 10% (solvent B) to 95% (solvent B) over 24 min and then held at 95% (solvent B) for 3 min. The analytical column was maintained at 40 °C throughout the run. The nebulizing gas (N_2) was set at a pressure of 35 psi during separation following voltage application. The source capillary voltage was set at 4,000 V with the drying gas at a flow rate of 5 l min^{-1} and at a temperature of 230 °C. For all PFAS standards, data acquisition was performed in dynamic multiple reaction monitoring mode under optimal fragmentation voltages.

An Agilent 8890 GC equipped with an Agilent HP-5ms low-bleed column (30 m, 0.25 mm internal diameter, 0.25-μm film) using He carrier gas for liquid and headspace sampling was used for GC-MS analysis. A tandem Agilent 5977B mass selective detector is used for liquid and headspace gas analysis.

Raman spectra were collected with a Renishaw Raman microscope using a 532 nm laser with a power of 5 mW. A 50× lens was used to collect all spectra. Analysis of Raman spectra, including peak intensity ratios, utilizes the height of the peak. Among these, 200 measurements were taken, and only those with a discernable G peak were considered for analysis (commonly ~99% of the spectra collected). This avoids using unfocused measurements. Custom Python scripts[51] were used to analyse Raman spectral mapping data by comparing peak intensity ratios and peak height. Graphene yield was calculated using I_{2D}/I_G ratios from these analyses. We looked for the $I_{2D}/I_G > 0.3$ and then divided those ratios by the total number of spectra collected to give the graphene yield.

Powder XRD spectra were collected using a Rigaku SmartLab II using Powder XRD measurements were done on a Rigaku SmartLab Intelligent XRD system with filtered Cu Kα radiation (λ = 1.5406 Å) zero background sample holders were used along at a scan rate of 5° min^{-1} and a 0.02° step size.

XPS data were collected using a PHI quantera SXM scanning X-ray microprobe with a base pressure of 5×10^{-9} Torr. Survey spectra were recorded using 0.5 eV step sizes with a pass energy of 140 eV. Elemental spectra were recorded using 0.1 eV step sizes with a pass energy of 26 eV. All the XPS spectra were corrected using the C 1*s* peaks (284.8 eV) as reference. Nexsa G2 XPS was used for surface and elemental analysis of Supplementary Fig. 24.

Scanning electron microscopy (SEM) images were taken with an FEI Helios Nanolab 660 Dual Beam SEM System. A voltage of 15 keV, a beam current of 100 pA and a working distance of 4 mm were used for imaging. High-resolution transmission electron microscopy and high-angle annular dark-field scanning transmission electron microscopy images were taken with the FEI Titan Themis S/TEM instrument at 300 keV after accurate spherical aberration correction. Samples were prepared by drop-casting dilute F1DM/ethanol solutions onto lacey carbon grids.

The NMR spectra were taken using Bruker NEO 600 MHz High Performance Digital NMR with a helium-cooled inverse TCI 600S3 H&F/CN-D-05 ZXT probe. The sample temperature ranges from −40 to 150 °C. The probe's sensitivity is based on the ^{19}F signal-to-noise ratio of 7,000:1. For NMR characterization the samples were rinsed with deionized water and D_20 wash added to form a 3:1 ratio. The position and shift of the F peaks depend on the level of solvation and deshielding the atoms experience[52].

The Mitsubishi AQF-2100H Furnace System was used to combust ~5 mg of sample in a ceramic boat ($n = 3$). Each boat, loaded with the stock reactant, was conveyed to the end position of the pyrolysis tube in the furnace by a solid sample changer (ABC-210) at a boat speed of 20 mm s^{-1} and combusted for 10 min. The inlet and outlet temperatures of the furnace were set at 900 °C and 1,000 °C, respectively. Oxygen and argon were introduced into the furnace at 400 ml min^{-1} and 200 ml min^{-1}, respectively. Ultrapure water (18.2 MΩ cm) was introduced into the furnace at a rate of 100 μl min^{-1} to aid in dissolving the generated hydrogen fluoride or fluorine gas from the furnace. The absorption solutions were subsequently analysed for fluoride concentrations using a Dionex ICS-ion chromatography system equipped with a Dionex AERS 500 suppressor (2 mm, Thermo Scientific) and a Dionex IonPac AS28 column (2 × 150 mm, 4-μm particle size). The eluent was 55 mM KOH at a flow rate of 0.1 ml min^{-1}. Aliquots of 1,000 mg l^{-1} fluoride stock solutions were employed to calibrate the IC. The retention time for fluoride was 7.3 min. The total chromatographic run time was 20 min. The average starting concentration was (0.951 ± 0.022) wt% of fluoride ($n = 3$ and $R^2 = 0.9980$).

The filtrates of the washed samples post-FJH were diluted using 2% HNO_3 and analysed using inductively coupled plasma mass spectrometry (ICP-MS). For the extraction of neat GAC, 100 mg of GAC was digested using 30 ml of 2% HNO_3 at room temperature for 24 h. The filtrate was further diluted and analysed. The Cu, Zn, Si, Al and Fe were measured by ICP-MS using a Perkin Elmer Nexion 2000B ICP-MS system with Periodic Table Mix 1 for ICP (10 mg l^{-1}, 10 wt% HNO_3, MilliporeSigma) as the standard. The standard solutions were prepared with 1, 5, 10, 25, 50, 100 ppb concentrations by diluting the original Mix 1 solution with 2 wt% HNO_3 solution. The sample concentration was calculated from the calibration curve. The sample was diluted to the appropriate concentration using 2 wt% HNO_3 within the calibration curve range.

Materials

PFOA adsorbed onto GAC was obtained from the Army Corps of Engineers-Engineer Research and Development Center (ERDC), and the GAC (Filtrasorb 400 or F400) was purchased from Chemviron Carbon. Activated charcoal used for solid-state dilution was obtained from MilliporeSigma (product ID 242268-250 G). Solid PFOA was obtained from SynQuest Laboratory. $Ca(OH)_2$ was purchased from Fisher Scientific (C97-500). NaOH was obtained from MilliporeSigma (367176-2KG) and VWR IC PolyVials, 10571-344, from Avantor. F^- standard (1,000 mg l^{-1}) was obtained from MilliporeSigma (2121-3-18). Carbon black (APS 10 nm, Black Pearls 2000) was purchased from Cabot Corporation. PFOS potassium salt was purchased from MilliporeSigma (2795-39-3). PTFE was purchased from Runaway Bike. American Chemical

Society-grade methanol for cleaning between reactions was purchased from MilliporeSigma (179337).

LCA and TEA

The LCA and TEA were conducted using OpenLCA[53] and GREET[54] software. The energy is calculated based on report values for the reaction process. CO_2 emissions are calculated based on electricity, materials used/consumed and products. More details can be found in Supplementary Section 8.

Atomistic modelling

Density functional theory (DFT) methods[55] are used as implemented in the Vienna ab initio simulation package (VASP)[56]. A plane wave expansion up to 500 eV is employed in combination with an all-electron-like projector-augmented wave potential[57]. Exchange correlation is treated within the generalized gradient approximation using the functional parameterized by Perdew–Burke–Ernserhof[58]. Because all the supercells are big enough with the smallest one being 15.0 Å × 15.0 Å × 22.0 Å, only Γ point is used for the Brillouin zone integration over Monkhorst–Pack-type mesh[59]. In structure optimization using the conjugate–gradient algorithm as implemented in VASP, both the positions of atoms and the unit cells are fully relaxed so that the maximum force on each atom is smaller than 0.01 eV $Å^{-1}$. For modelling of the catalytic reaction, the optimized structures are subsequently annealed for 30 ps with the temperature fluctuating at the range of 1,500–2,500 K in MD simulation. The MD simulation is performed using a Nose–Hoover thermostat and under conditions where the number of particles (N), volume (V), and temperature (T) are kept constant (NVT ensemble) with a time step of 0.5 fs. Because the catalytic reaction leads to the cleavage of the F–C bonds in the PFAS molecules, the number of C–F bonds were used in the system as a descriptor of the catalytic effect. The number of unbroken C–F bonds was calculated every 20 steps (10 fs) in each of the MD simulations, and the results are shown in Fig. 4a,b. In counting the number of C–F bonds, the cut-off distance is set at 1.55 Å as compared to the equilibrium C–F bond length of 1.40 Å.

Reporting summary

Further information on research design is available in the Nature Portfolio Reporting Summary linked to this article.

Data availability

Supplementary datasets for Monte Carlo LCA and TEA calculations are available via Zenodo at https://doi.org/10.5281/zenodo.14852070 (ref. 60).

Code availability

Custom Python scripts were used to analyse Raman spectral mapping data by comparing peak intensity ratios and peak height. These scripts are available via Github at https://github.com/jlb48249/FJH_ML.

References

1. Al Amin, M. D. et al. Recent advances in the analysis of per- and polyfluoroalkyl substances (PFAS)—a review. *Environ. Technol. Innovation* **19**, 100879 (2020).
2. Glüge, J. et al. An overview of the uses of per- and polyfluoroalkyl substances (PFAS). *Environ. Sci. Processes Impacts* **22**, 2345–2373 (2020).
3. Hunter Anderson, R., Adamson, D. T. & Stroo, H. F. Partitioning of poly- and perfluoroalkyl substances from soil to groundwater within aqueous film-forming foam source zones. *J. Contam. Hydrol.* **220**, 59–65 (2019).
4. Xiao, X., Ulrich, B. A., Chen, B. & Higgins, C. P. Sorption of poly- and perfluoroalkyl substances (PFASs) relevant to aqueous film-forming foam (AFFF)-impacted groundwater by biochars and activated carbon. *Environ. Sci. Technol.* **51**, 6342–6351 (2017).
5. Stahl, T., Mattern, D. & Brunn, H. Toxicology of perfluorinated compounds. *Environ. Sci. Eur.* **23**, 38 (2011).
6. Sunderland, E. M. et al. A review of the pathways of human exposure to poly- and perfluoroalkyl substances (PFASs) and present understanding of health effects. *J. Exposure Sci. Environ. Epidemiol.* **29**, 131–147 (2018).
7. Sonmez Baghirzade, B. et al. Thermal regeneration of spent granular activated carbon presents an opportunity to break the forever PFAS cycle. *Environ. Sci. Technol.* **55**, 5608–5619 (2021).
8. Yeung, L. W. et al. Perfluorinated compounds and total and extractable organic fluorine in human blood samples from China. *Environ. Sci. Technol.* **42**, 8140–8145 (2008).
9. Aro, R., Eriksson, U., Kärrman, A. & Yeung, L. W. Organofluorine mass balance analysis of whole blood samples in relation to gender and age. *Environ. Sci. Technol.* **55**, 13142–13151 (2021).
10. Buck, R. C. et al. Perfluoroalkyl and polyfluoroalkyl substances in the environment: terminology, classification, and origins. *Integr. Environ. Assess. Manage.* **7**, 513–541 (2011).
11. Ellis, D. A., Mabury, S. A., Martin, J. W. & Muir, D. C. Thermolysis of fluoropolymers as a potential source of halogenated organic acids in the environment. *Nature* **412**, 321–324 (2001).
12. Brusseau, M. L., Anderson, R. H. & Guo, B. PFAS concentrations in soils: background levels versus contaminated sites. *Sci. Total Environ.* **740**, 140017 (2020).
13. Scher, D. P. et al. Occurrence of perfluoroalkyl substances (PFAS) in garden produce at homes with a history of PFAS-contaminated drinking water. *Chemosphere* **196**, 548–555 (2018).
14. Xiao, F., Hanson, R. A., Golovko, S. A., Golovko, M. Y. & Arnold, W. A. PFOA and PFOS are generated from zwitterionic and cationic precursor compounds during water disinfection with chlorine or ozone. *Environ. Sci. Technol. Lett.* **5**, 382–388 (2018).
15. Belkouteb, N., Franke, V., McCleaf, P., Köhler, S. & Ahrens, L. Removal of per- and polyfluoroalkyl substances (PFASs) in a full-scale drinking water treatment plant: long-term performance of granular activated carbon (GAC) and influence of flow-rate. *Water Res.* **182**, 115913 (2020).
16. *Per- and Polyfluoroalkyl Substances (PFAS) Proposed PFAS National Primary Drinking Water Regulation* (US EPA, 2023); https://www.epa.gov/sdwa/and-polyfluoroalkyl-substances-pfas#:~:text=On%20March%2014%2C%202023%20%2C%20EPA,known%20as%20GenX%20Chemicals)%2C%20perfluorohexane
17. Gagliano, E., Falciglia, P. P., Zaker, Y., Karanfil, T. & Roccaro, P. Microwave regeneration of granular activated carbon saturated with PFAS. *Water Res.* **198**, 117121 (2021).
18. McCleaf, P. et al. Removal efficiency of multiple poly- and perfluoroalkyl substances (PFASs) in drinking water using granular activated carbon (GAC) and anion exchange (AE) column tests. *Water Res.* **120**, 77–87 (2017).
19. Dastgheib, S. A., Mock, J., Ilangovan, T. & Patterson, C. Thermogravimetric studies for the incineration of an anion exchange resin laden with short- or long-chain PFAS compounds containing carboxylic or sulfonic acid functionalities in the presence or absence of calcium oxide. *Ind. Eng. Chem. Res.* **60**, 16961–16968 (2021).
20. Xiao, F. et al. Thermal stability and decomposition of perfluoroalkyl substances on spent granular activated carbon. *Environ. Sci. Technol. Lett.* **7**, 343–350 (2020).
21. Watanabe, N., Takemine, S., Yamamoto, K., Haga, Y. & Takata, M. Residual organic fluorinated compounds from thermal treatment of PFOA, PFHxA and PFOS adsorbed onto granular activated carbon (GAC). *J. Mater. Cycles Waste Manage.* **18**, 625–630 (2016).
22. Feng, M. et al. Characterization of the thermolysis products of Nafion membrane: a potential source of perfluorinated compounds in the environment. *Sci. Rep.* **5**, 9859 (2015).

23. Stoiber, T., Evans, S. & Naidenko, O. V. Disposal of products and materials containing per- and polyfluoroalkyl substances (PFAS): a cyclical problem. *Chemosphere* **260**, 127659 (2020).
24. Martin, K. V. et al. PFAS soil concentrations surrounding a hazardous waste incinerator in East Liverpool, Ohio, an environmental justice community. *Environ. Sci. Pollut. Res.* **30**, 80643–80654 (2023).
25. Wang, B. et al. Per- and polyfluoroalkyl substances and the contribution of unknown precursors and short-chain (C2–C3) perfluoroalkyl carboxylic acids at solid waste disposal facilities. *Sci. Total Environ.* **705**, 135832 (2020).
26. Loganathan, B. G., Sajwan, K. S., Sinclair, E., Senthil Kumar, K. & Kannan, K. Perfluoroalkyl sulfonates and perfluorocarboxylates in two wastewater treatment facilities in Kentucky and Georgia. *Water Res.* **41**, 4611–4620 (2007).
27. *National Defense Authorization Act for Fiscal Year 2020* (116th US Congress, 2019); https://www.congress.gov/116/plaws/publ92/PLAW-116publ92.pdf
28. Abou-Khalil, C. et al. Enhancing the thermal mineralization of perfluorooctanesulfonate on granular activated carbon using alkali and alkaline-earth metal additives. *Environ. Sci. Technol.* **58**, 11162–11174 (2024).
29. Xiao, F., Challa Sasi, P., Alinezhad, A., Sun, R. & Abdulmalik Ali, M. Thermal phase transition and rapid degradation of forever chemicals (PFAS) in spent media using induction heating. *Environ. Sci. Technol.* **3**, 1370–1380 (2023).
30. Singh, R. K. et al. Breakdown products from perfluorinated alkyl substances (PFAS) degradation in a plasma-based water treatment process. *Environ. Sci. Technol.* **53**, 2731–2738 (2019).
31. Algozeeb, W. A. et al. Flash graphene from plastic waste. *ACS Nano* **14**, 15595–15604 (2020).
32. Cheng, Y. et al. Flash upcycling of waste glass fibre-reinforced plastics to silicon carbide. *Nat. Sustainability* **7**, 452–462 (2024).
33. Dong, S. et al. Ultra-fast, low-cost, and green regeneration of graphite anode using flash Joule heating method. *EcoMat* **4**, e12212 (2022).
34. Deng, B. et al. High-temperature electrothermal remediation of multi-pollutants in soil. *Nat. Commun.* **14**, 6371 (2023).
35. Cheng, Y. et al. Electrothermal mineralization of per- and polyfluoroalkyl substances (PFAS) for soil remediation. *Nat. Commun.* **15**, 6117 (2024).
36. Eddy, L. et al. Electric field effects in flash Joule heating synthesis. *J. Am. Chem. Soc.* **146**, 16010–16019 (2024).
37. Luong, D. X. et al. Gram-scale bottom-up flash graphene synthesis. *Nature* **577**, 647–651 (2020).
38. Crosby, N. T. Equilibria of fluorosilicate solutions with special reference to the fluoridation of public water supplies. *J. Appl. Chem.* **19**, 100–102 (2007).
39. Suzuki, Y., Park, T., Hachiya, K. & Goto, T. Raman spectroscopy for determination of silicon oxyfluoride structure in fluoride melts. *J. Fluorine Chem.* **238**, 109616 (2020).
40. Puts, G., Crouse, P. & Ameduri, B. Polytetrafluoroethylene: synthesis and characterization of the original extreme polymer. *Chem. Rev.* **119**, 1763–1805 (2019).
41. Chen, W. et al. Heteroatom-doped flash graphene. *ACS Nano* **16**, 6646–6656 (2022).
42. Finnveden, G. et al. Recent developments in life cycle assessment. *J. Environ. Manage.* **91**, 1–21 (2009).
43. Guinée, J. B. et al. Life cycle assessment: past, present, and future. *Environ. Sci. Technol.* **45**, 90–96 (2011).
44. Hellweg, S. & Milà i Canals, L. Emerging approaches, challenges and opportunities in life cycle assessment. *Science* **344**, 1109–1113 (2014).
45. Zhang, K. et al. Destruction of perfluorooctane sulfonate (PFOS) and perfluorooctanoic acid (PFOA) by ball milling. *Environ. Sci. Technol.* **47**, 6471–6477 (2013).
46. Siriwardena, D. P. et al. Regeneration of per- and polyfluoroalkyl substance-laden granular activated carbon using a solvent based technology. *J. Environ. Manage.* **289**, 112439 (2021).
47. This changes everything… *Universal Matter* https://www.universalmatter.com/ (2024).
48. Wyss, K. M. et al. Synthesis of clean hydrogen gas from waste plastic at zero net cost. *Adv. Mater.* **35**, 2306763 (2023).
49. Wyss, K. M., Deng, B. & Tour, J. M. Upcycling and urban mining for nanomaterial synthesis. *Nano Today* **49**, 101781 (2023).
50. Eddy, L. et al. Automated laboratory kilogram-scale graphene production from coal. *Small Methods* **8**, 2301144 (2023).
51. Beckham, J. L. et al. Machine learning guided synthesis of flash graphene. *Adv. Mater.* **34**, 2106506 (2022).
52. Gerken, M. et al. The NMR shifts are not a measure for the nakedness of the fluoride anion. *J. Fluorine Chem.* **116**, 49–58 (2002).
53. Leaders in LCA and sustainability assessment. *OpenLCA* https://www.openlca.org/ (2025).
54. GREET. *US Department of Energy* https://www.energy.gov/eere/greet/ (1995).
55. Dudarev, S. L., Botton, G. A., Savrasov, S. Y., Humphreys, C. J. & Sutton, A. P. Electron-energy-loss spectra and the structural stability of nickel oxide: an LSDA+U study. *Phys. Rev. B* **57**, 1505–1509 (1998).
56. Kresse, G. & Furthmüller, J. Efficient iterative schemes for ab initio total-energy calculations using a plane-wave basis set. *Phys. Rev. B* **54**, 11169–11186 (1996).
57. Blöchl, P. E. Projector augmented-wave method. *Phys. Rev. B* **50**, 17953–17979 (1994).
58. Perdew, J. P., Burke, K. & Ernzerhof, M. Generalized gradient approximation made simple. *Phys. Rev. Lett.* **77**, 3865–3868 (1996).
59. Monkhorst, H. J. & Pack, J. D. Special points for Brillouin-zone integrations. *Phys. Rev. B* **13**, 5188–5192 (1976).
60. Scotland, P. et al. Mineralization of captured perfluorooctanoic acid and perfluorooctane sulfonic acid at zero net cost using flash Joule heating. *Zenodo* https://doi.org/10.5281/zenodo.14852070 (2025).

Acknowledgements

The funding of the research is provided by Air Force Office of Scientific Research (FA9550-22-1-0526, J.M.T.), US Army Corps of Engineers, ERDC (W912HZ-21-2-0050, J.M.T., B.I.Y., Y.Z., S.G.Z., C.G.), the National Science Foundation Graduate Research Fellowship Program (J.L.B.), the Stauffer–Rothwell Scholarship from Rice University (K.M.W.) and Rice Academy Fellowship (Y.C.). Computer resources were provided through the US Department of Energy award (BES-ERCAP0027822, B.I.Y.). C.-H.C. and Y.H. acknowledge Welch Foundation (C-2065), and American Chemical Society Petroleum Research Fund (67236-DNI10). Permission to publish was granted by Director, Geotechnical and Structures Laboratory, ERDC. We acknowledge and thank A. Kimble and J. Puhnaty from ERDC, who contributed to the preparation of the PFOA-GAC used in this work. B. Chen aided in the XPS analysis. We acknowledge C. Kittrell for his advice and support in the early stages on this project. The characterization equipment used in this project is partly from the Shared Equipment Authority and the Electron Microscopy Core at Rice University.

Author contributions

P.S. conceived the idea to use sodium as a mineralizing agent for PFOA, PFOS and PTFE, conducted IC, LCMS, CIC, NMR, XRD, XPS, TEA and paper writing under the guidance of J.M.T. K.M.W performed GC-MS, Raman spectroscopy and contributed to the experimental design ideas and LCA. Y. Cheng aided with experimental design and

experiments, L.E. contributed to initial experiment testing. J.L.B. contributed to Raman analysis and paper writing. J.S. contributed to the LCA and TEA. C.H.C. performed TEM characterization. T.S. contributed to NMR analysis. Y. Chung and B.W. contributed to IC and LCMS. Y.-Y.S. and J.A.D. contributed to IC. B.D. contributed to experimental design ideas and part of the reaction schematics. Y.Z. contributed to DFT and computational data. Y.H. supervised C.H.C. in performing TEM characterization. B.I.Y. supervised Y.Z. in performing computational experiments. M.S.W. supervised Y.C. B.W. and J.A.D. M.T. supervised Y.-Y.S. S.G.Z. and C.G. contributed PFAS-adsorbed GAC samples. J.M.T. supervised P.S. for all the process, guided P.S. in paper writing and oversaw the entire project.

Competing interests

Intellectual property (IP) has been filed by Rice University on the FJH strategy for PFAS destruction, which is being licensed to companies in which J.M.T. is a shareholder, but not an officer, director or employee. Conflicts of interest are mitigated by disclosure to and compliance with the Office of Sponsored Programs and Research Compliance at Rice University. The other authors declare no competing interests.

Additional information

Extended data is available for this paper at https://doi.org/10.1038/s44221-025-00404-z.

Supplementary information The online version contains supplementary material available at https://doi.org/10.1038/s44221-025-00404-z.

Correspondence and requests for materials should be addressed to Yufeng Zhao or James M. Tour.

Peer review information *Nature Water* thanks Feng Xiao and the other, anonymous, reviewer(s) for their contribution to the peer review of this work.

---

[1]Department of Materials Science and Nanoengineering, Rice University, Houston, TX, USA. [2]Department of Chemistry, Rice University, Houston, TX, USA. [3]Smalley-Curl Institute, Rice University, Houston, TX, USA. [4]Department of Applied Physics, Rice University, Houston, TX, USA. [5]Department of Chemical and Biomolecular Engineering, Rice University, Houston, TX, USA. [6]Nanosystems Engineering Research Center for Nanotechnology-Enabled Water Treatment, Houston, TX, USA. [7]Rice Water Technologies, Entrepreneurship and Research (WaTER) Institute, Houston, TX, USA. [8]Rice Sustainability Institute, Houston, TX, USA. [9]Department of Civil and Environmental Engineering, Rice University, Houston, TX, USA. [10]US Army Engineer Research and Development Center, Vicksburg, MS, USA. [11]Corban University, Salem, OR, USA. [12]NanoCarbon Center and Rice Advanced Materials Institute, Rice University, Houston, TX, USA. ✉e-mail: yzhao@corban.edu; tour@rice.edu

https://doi.org/10.1038/s44221-025-00404-z

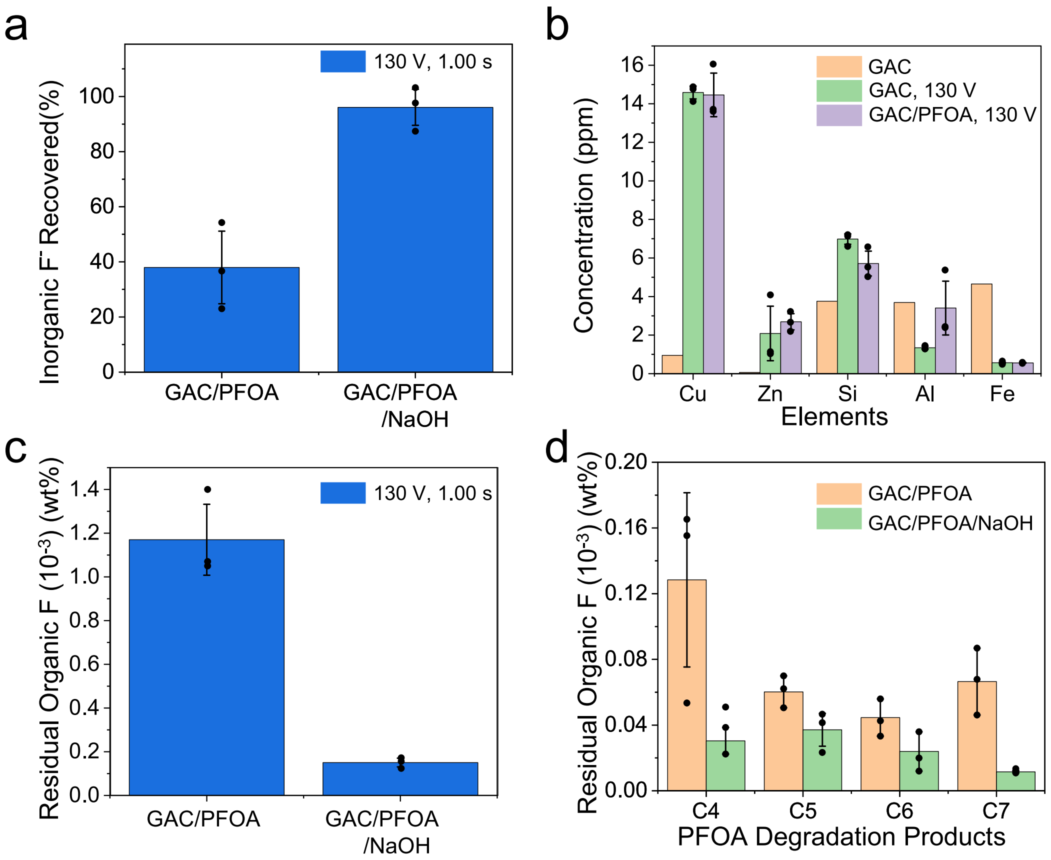

Extended Data Fig. 1 | Quantification of inorganic and organic F. a) Ion chromatography results of 0.1 g of GAC/PFOA and GAC/PFOA/x1.2Na after FJH, (n = 3 for all samples). **b)** Inductive Couple Plasma-Mass spectrometry (ICP-MS) of the filtrate of i) neat GAC (n = 1), ii) GAC/130 V (n = 3), and iii) GAC/PFOA/130 V (n = 3). **c)** LCMS quantification of the remaining organic F derived from PFOA. **d)** LCMS results of the GAC/PFOA and GAC/PFOA/NaOH when FJH at 130 V for 1.00 s. The data in 1a, 1b ii-iii, and 1 d are presented as the mean ± s.d. of the LCMS results from 3 parallel experiments (n = 3).

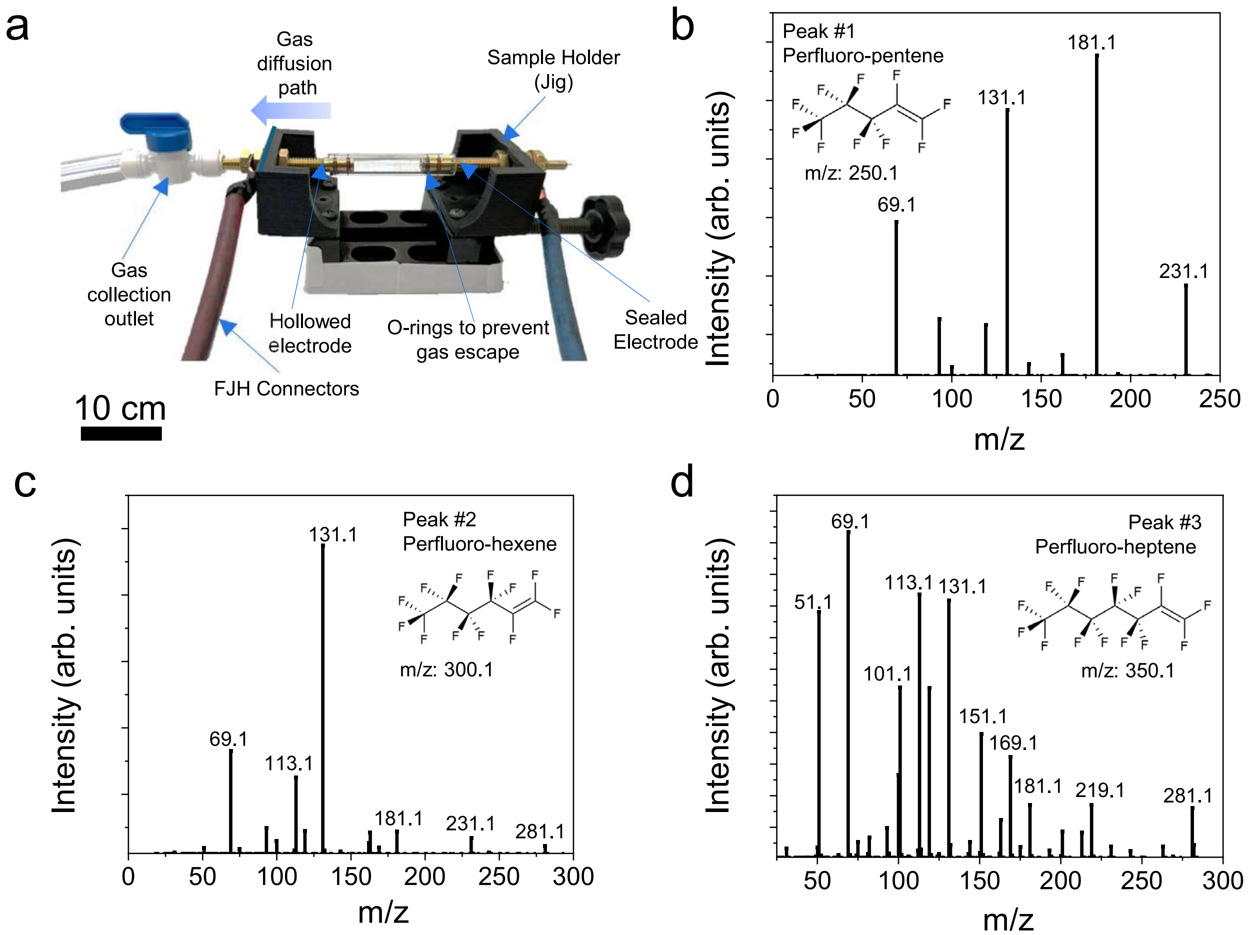

Extended Data Fig. 2 | Gas chromatograph mass spectrometry (GC-MS) analysis of reaction byproducts. a) A picture of the gas capture setup to collect gases evolved by flash Joule heating. A perforated brass electrode allows for the capture of gases evolved during the reaction. The captured gases are then analyzed using GC-MS to probe possible perfluorocarbon production during the PFOA degradation process. The instrumental scan resolution was set to end at 300 m/z, so higher mass fragments were not observed. **b)** Mass spectrum of peak #1, the perfluoro pentene peak. **c**) Mass spectrum of peak #2, the perfluoro hexene peak. **d)** Mass spectrum of peak #3, the perfluoro heptene peak, the decarboxylated parent PFOA peak.

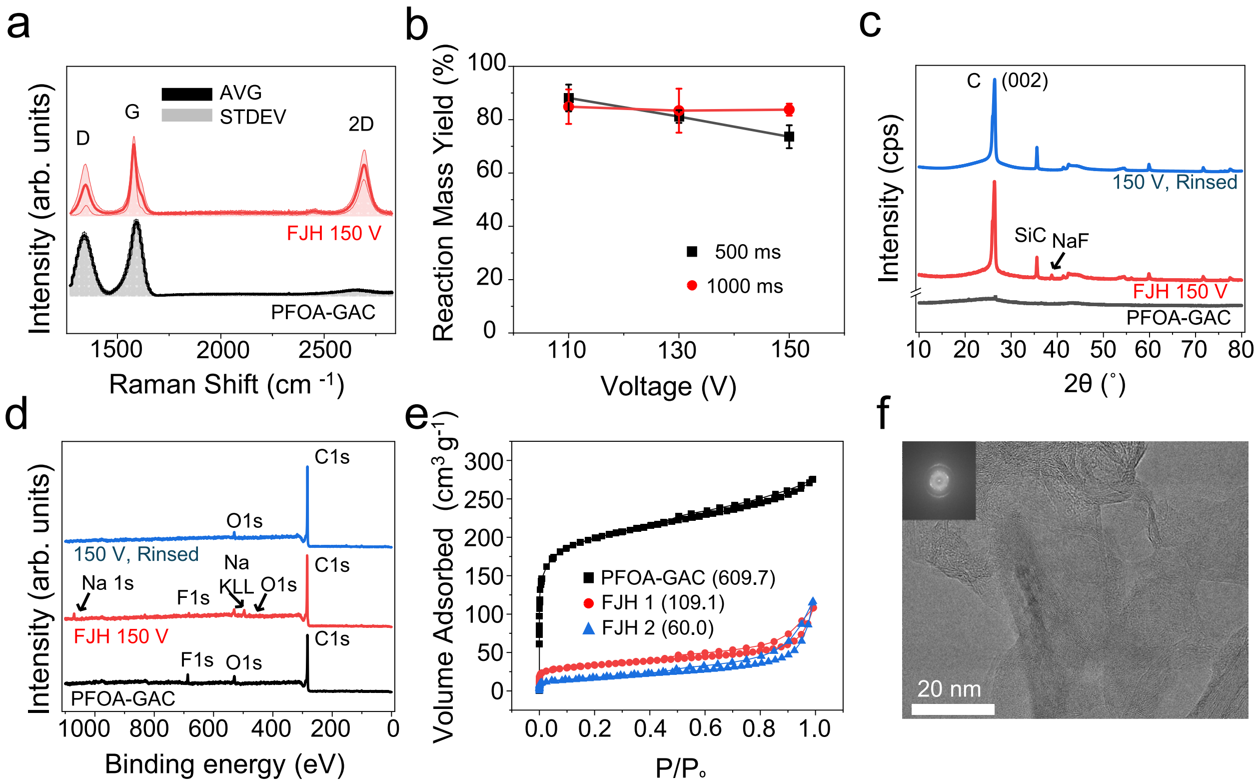

Extended Data Fig. 3 | Characterization of the reactants and FJH reaction products. a) Statistic Raman spectrum of PFOA-GAC starting material and optimized GAC-derived flash graphene (FG) product that was FJH at 150 V and 1.00 s. The solid line and colored shadows represent the average value and standard deviation of 100 sampling points, respectively. **b)** Reaction mass yield with respect to reaction voltage at two different pulse times. The data are presented as the mean ± s.d. of the reaction mass yield from 3 parallel experiments (n = 3). **c)** XRD spectra of the raw materials and FJH products before and after rinsing (Powder Diffraction File 00-041-1487, Graphite-2H and 01-080-8615, NaF). **d)** XPS survey spectra of the raw material and FJH products before and after rinsing. **e)** BET surface area analysis isotherms of the raw starting material GAC and the FJH reaction products. **f)** TEM analysis of the produced graphene. The inset shows an FFT of the highlighted area, the scale bar is the same as the TEM image.

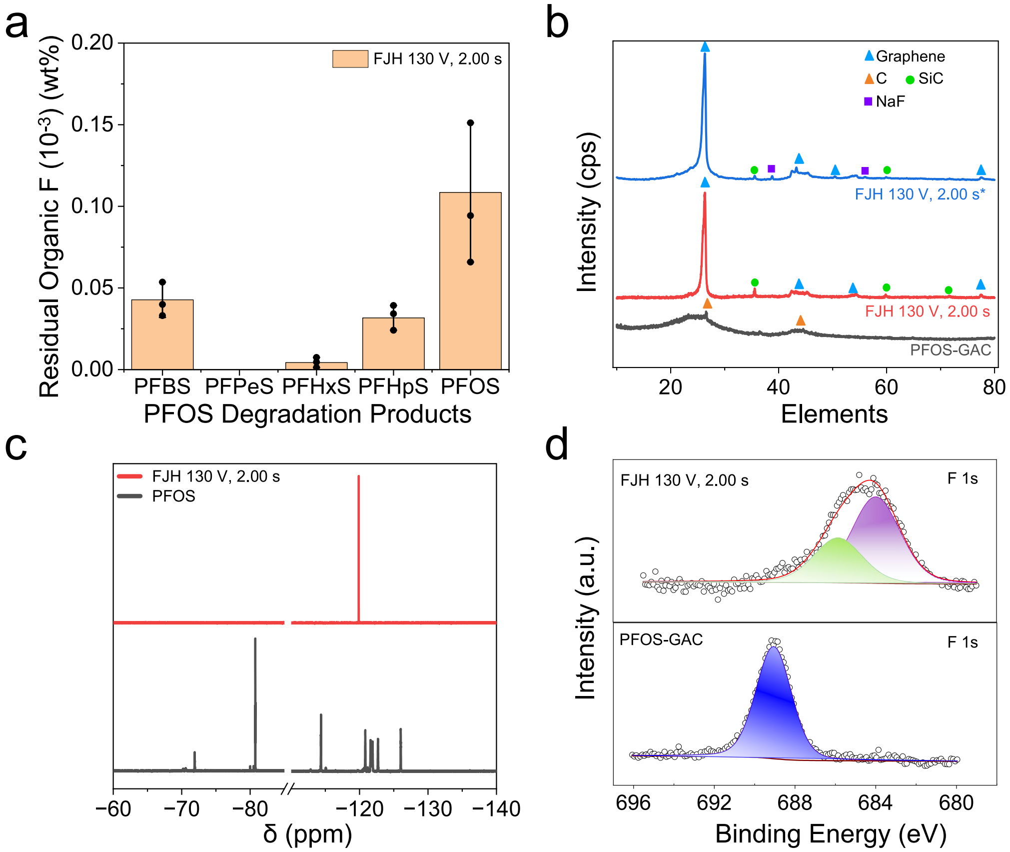

Extended Data Fig. 4 | Characterization of GAC/PFOS/Na before and after FJH. a) LCMS results for GAC/PFOS/Na FJH at 130 V for 2.00 s. The PFOS removal efficiency is 99.97%. The data are presented as the mean ± s.d. of the LCMS results from 3 parallel experiments (n = 3). **b)** XRD spectra of the raw materials and FJH products. The blue trace represents a sample containing a slightly higher loading of PFOS so that we can observe the NaF peaks in the XRD spectra. **c)** ^{19}F NMR spectra of the raw material and FJH products before and after rinsing, **d)** XPS elemental spectra of the raw material and FJH products.

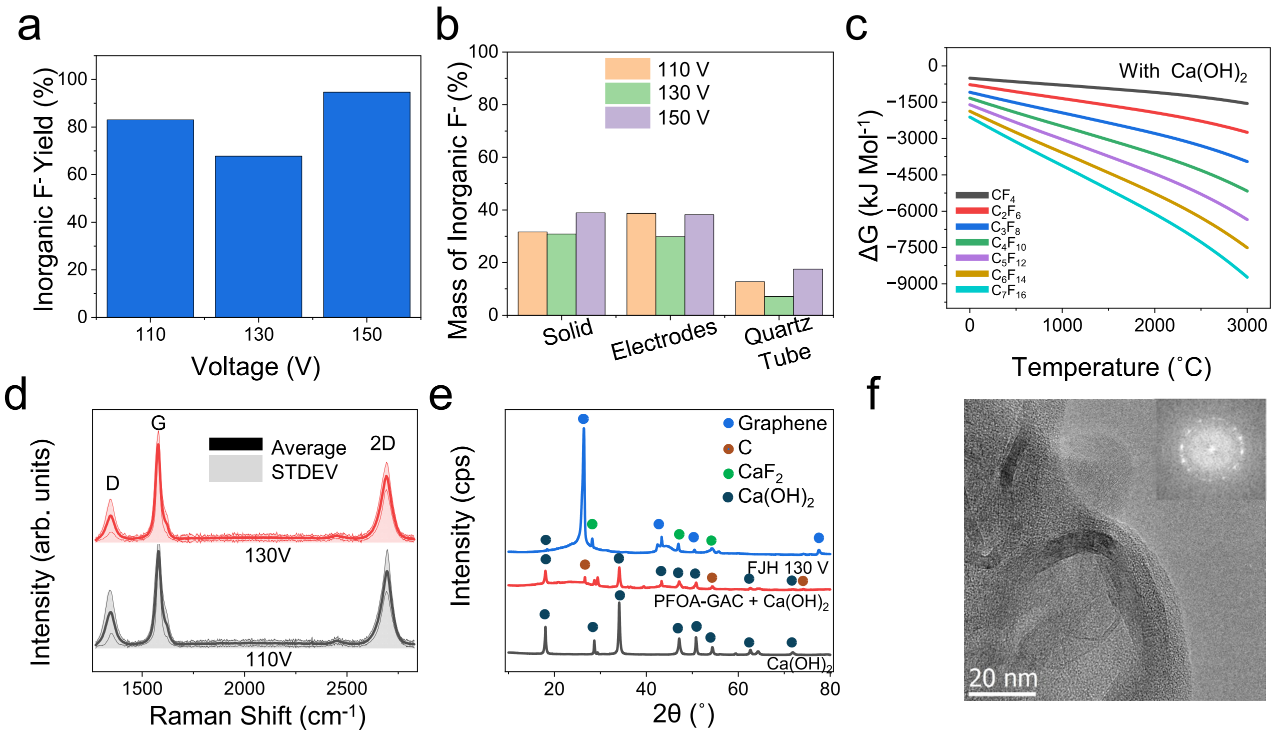

Extended Data Fig. 5 | Analysis of PFOA-GAC mixed with $Ca(OH)_2$ (0.5 calcium ions for every fluoride atom) and FJH at 110-150 V for 0.50 s. a-b) Ion chromatography analysis of the samples, post-FJH. 94% of elemental F present in the starting material is recovered as mineralized fluoride when FJH at 150 V (n = 1). One set of reactions was conducted as a proof of concept to limit the exposure of the sensitive analytical equipment to dilute H_2SO_4. **c)** Thermodynamics analysis using the HSC chemistry package shows that the mineralizing agent reacts readily with all fluorocarbons. This suggests that the addition of $Ca(OH)_2$ drives the mineralization process. **d)** The average Raman spectra of the 110 V and 130 V flash at 59 mF. The spectra were collected from 100 sampling points of the powdered product. The average D/G and 2D/G intensity ratios of the 110 V flash are 0.34 and 0.68, respectively. The graphene yield is 96%. The average D/G and 2D/G intensity ratios of the 130 V flashes are 0.25 and 0.72, respectively. The graphene yield is 98%. High-quality FG was produced. **e)** Bulk crystal structure analysis by XRD of the $Ca(OH)_2$, PFOA-GAC mixed with $Ca(OH)_2$, and the product after FJH at 130 V. The green circles highlight the CaF_2 phase. **f)** TEM image containing an FFT inset of the highlighted area shows turbostratic stacking of the domains and strong graphitic character with minimal amorphous character.

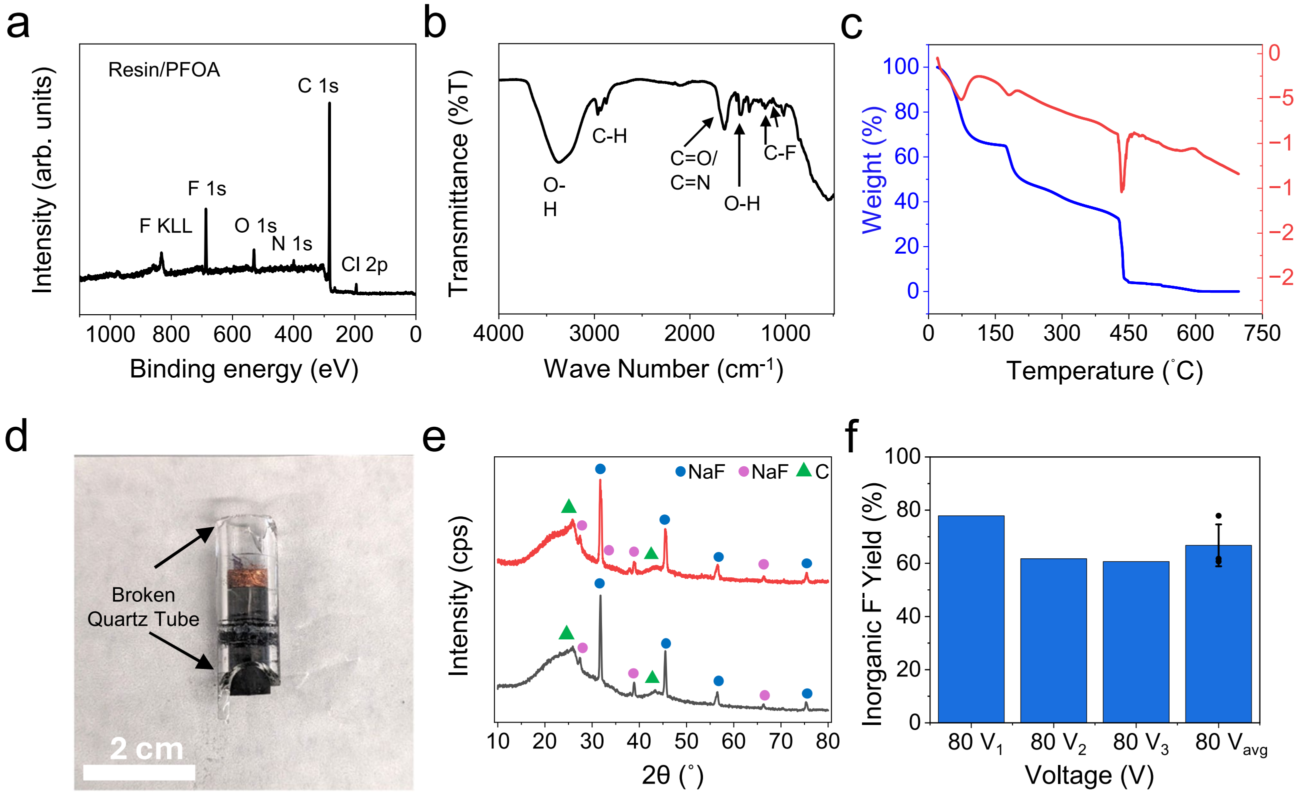

Extended Data Fig. 6 | Analysis of PFOA-Resin mixed with 2 molar eq of sodium per mole F in PFOA using NaOH, and FJH at 80 V for 1.00 s. a) XPS shows the high F content in the original PFOA-Resin. **b)** Fourier-transform infrared spectroscopy (FTIR) of the anion exchange resin with adsorbed PFOA. The C-F stretching vibration can be observed at 1204 and 1148 cm^{-1}. **c)** Thermal gravimetric analysis-differential scanning calorimetry (TGA-DSC) shows the various stages of weight loss of the resin. The first stage includes PFOA degradation followed by depolymerization of the resin then blackening. **d)** Reaction vessel after FJH. The sample shatters due to rapid gas formation and expansion. 80 V is the maximum voltage where the solid remains in the inner chamber and can be analyzed. **e)** XRD analysis of the post-reaction powder shows the presence of NaF. **f)** Ion chromatography results of the reactions. 66.7% of the PFOA is mineralized into inorganic NaF. The apparatus is a constraint of these samples as the glass tube shatters at high voltages. The data are presented as the mean ± s.d. of the IC results from 3 parallel experiments (n = 3).

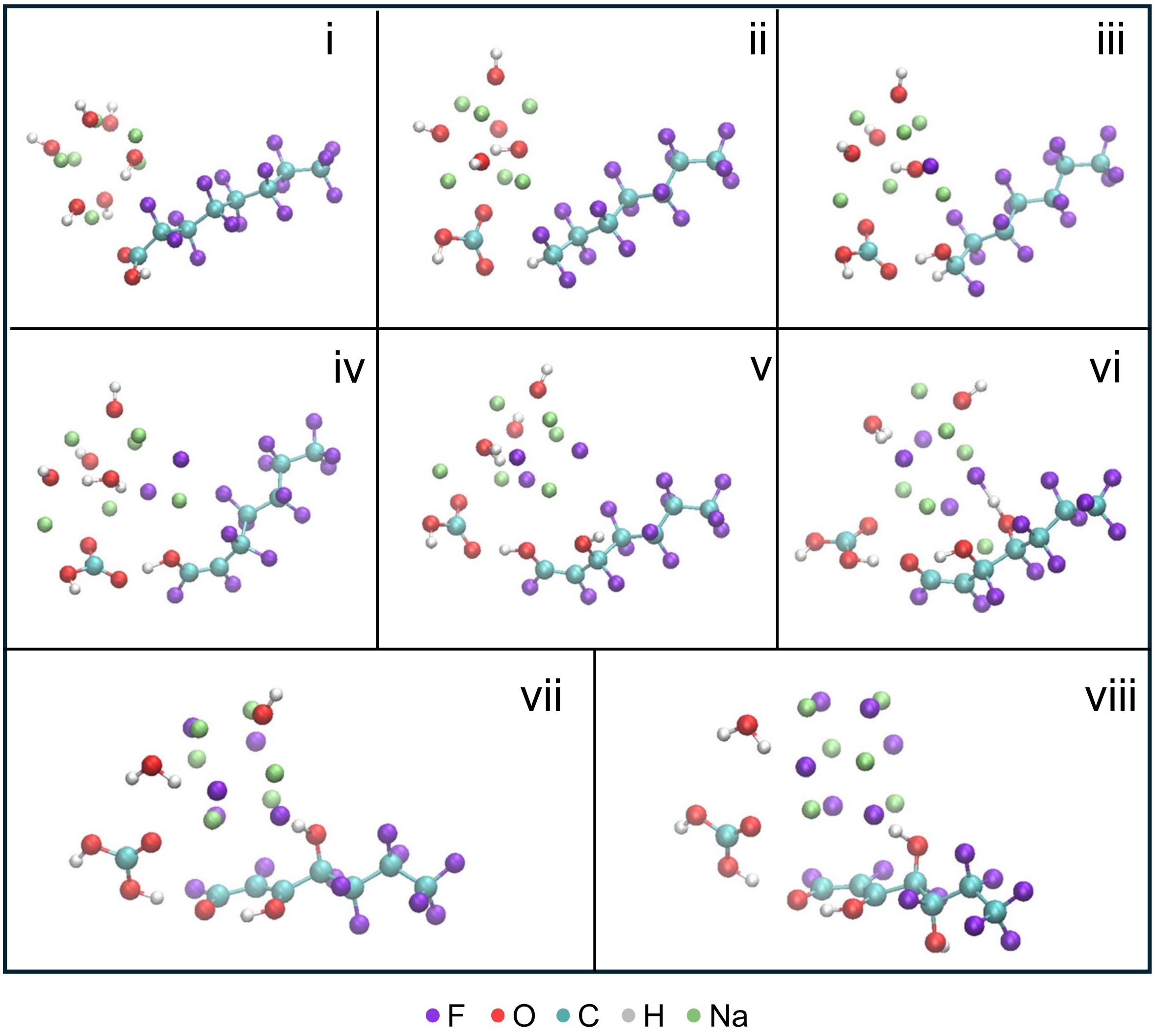

i) $6NaOH + HO_2C\text{-}C_7F_{15}$ → ii) $5NaOH + NaHCO_3 + H\text{-}C_7F_{15}$

→ iii) $4NaOH + NaHCO_3 + NaF + OH\text{-}H\text{-}C_7F_{14}$

→ iv) $3NaOH + NaHCO_3 + 2NaF + H_2O + HOFC{=}C_6F_{12}$

→ v) $2NaOH + NaHCO_3 + 3NaF + H_2O + HOFC{=}C_6F_{11}$

→ vi) $NaOH + H_2CO_3 + 4NaF + H_2O + NaOFC{=}(HO)_2\text{-}C_6F_{10}$

→ vii) $NaOH + H_2CO_3 + 5NaF + H_2O + FO{=}C\text{-}FC{=}C_5(HO)_2F_8$

→ viii) $H_2CO_3 + 6NaF + H_2O + FO{=}C\text{-}FC{=}C_5(HO)_3F_7$

Extended Data Fig. 7 | Molecular model depictions of the simulations, and the chemical equations derived from those simulations. Reaction Pathway 1 derived from Density Functional Theory (DFT) simulations.

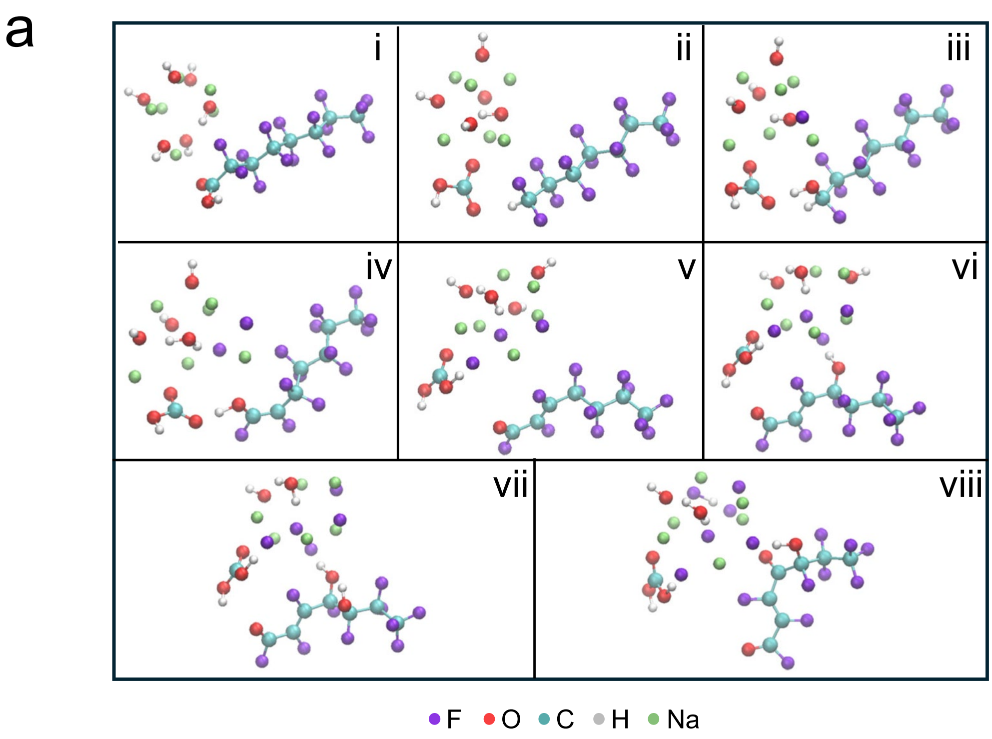

i) $6NaOH + HO_2C\text{-}C_7F_{15}$ → ii) $5NaOH + NaHCO_3 + H\text{-}C_7F_{15}$

→ iii) $4NaOH + NaHCO_3 + NaF + OH\text{-}H\text{-}C_7F_{14}$

→ iv) $3NaOH + NaHCO_3 + 2NaF + H_2O + HOFC{=}C_6F_{12}$

→ v) $3NaOH + H_2CO_3 + 3NaF + H_2O + FO{=}CF\text{-}CF{=}C_5F_9$

→ vi) $2NaOH + H_2CO_3 + 4NaF + H_2O + O{=}CF\text{-}FC{=}C_5HOF_9$

→ vii) $NaOH + H_2CO_3 + 5NaF + H_2O + O{=}CF\text{-}FC{=}C_5(HO)_2F_8$

→ viii) $NaOH + H_2CO_3 + 5NaF + H_2O + HF + O{=}CF\text{-}FC{=}CF\text{-}(C{=}O)\text{-}C_3(HO)F_6$

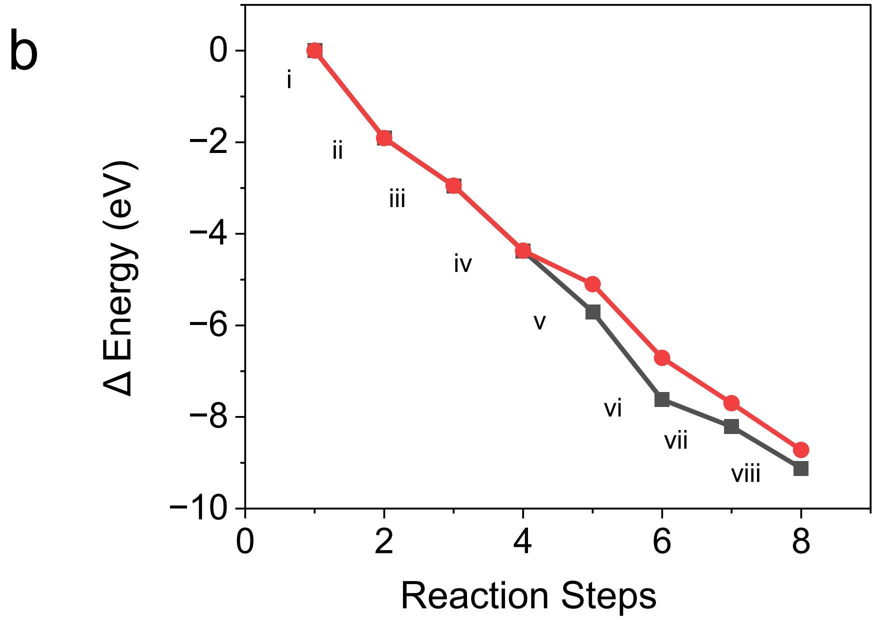

Extended Data Fig. 8 | See next page for caption.

Extended Data Fig. 8 | DFT simulations. a) Reaction Pathway 2 derived from DFT simulations. **b)** Energy calculations for the reaction steps of reaction pathways 1 and 2. The total energy goes down steadily step by step, which indicates that the above three rules of thumb are valid for energetics analysis. The reaction is driven by the reduction of F by Na. Because of the high electronegativity of F atoms, the F-C covalent bonds are highly frustrated, and the frustration can be released by replacing F with OH or removal of F through forming C = C double bonds.

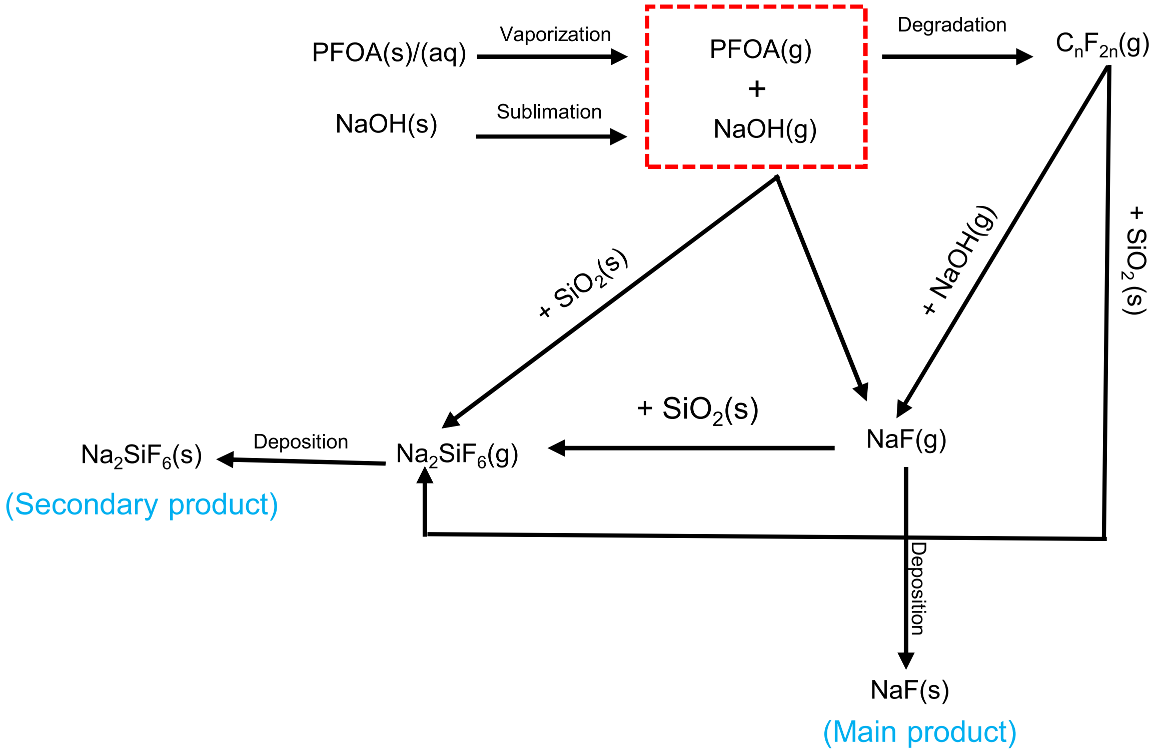

Extended Data Fig. 9 | Reaction pathways for production of NaF and Na_2SiF_6. Proposed reaction pathway for the degradation of PFOA in the presence of NaOH via FJH into inorganic fluorine salts.

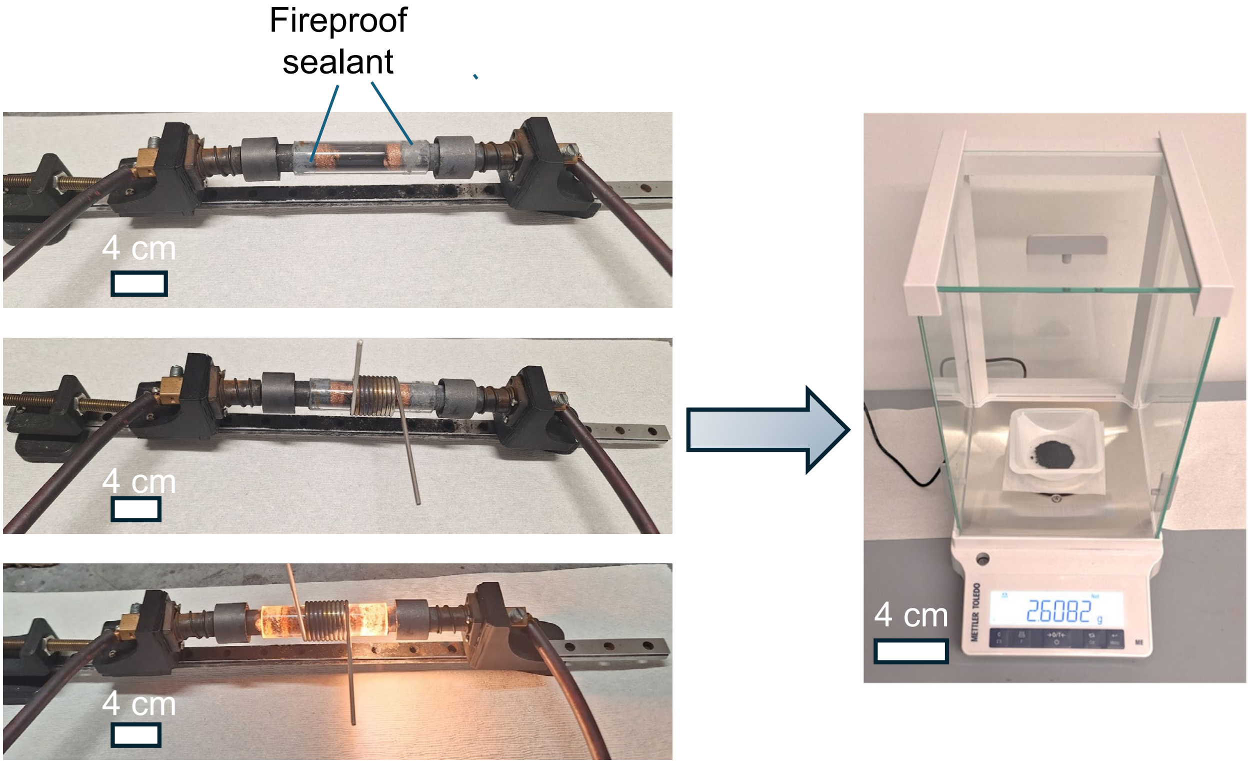

Extended Data Fig. 10 | Scaled up reaction to mineralize gram scale PFOA-GAC. This demonstrates our scale up technology in the lab to treat 3 g of PFOA on waste GAC. The starting PFOA concentration was 6.3 mg g^{-1} GAC. No short chain PFOA remained and the removal efficiency for PFOA was >99.9%. The balance shows that 2.6 g of graphene formed with small amounts of metal fluoride salts.

nature portfolio

Corresponding author(s): James M. Tour, Yufeng Zhao

Last updated by author(s): 02/05/2025

Reporting Summary

Nature Portfolio wishes to improve the reproducibility of the work that we publish. This form provides structure for consistency and transparency in reporting. For further information on Nature Portfolio policies, see our Editorial Policies and the Editorial Policy Checklist.

Statistics

For all statistical analyses, confirm that the following items are present in the figure legend, table legend, main text, or Methods section.

n/a	Confirmed	
☐	☒	The exact sample size (n) for each experimental group/condition, given as a discrete number and unit of measurement
☐	☒	A statement on whether measurements were taken from distinct samples or whether the same sample was measured repeatedly
☒	☐	The statistical test(s) used AND whether they are one- or two-sided *Only common tests should be described solely by name; describe more complex techniques in the Methods section.*
☒	☐	A description of all covariates tested
☒	☐	A description of any assumptions or corrections, such as tests of normality and adjustment for multiple comparisons
☒	☐	A full description of the statistical parameters including central tendency (e.g. means) or other basic estimates (e.g. regression coefficient) AND variation (e.g. standard deviation) or associated estimates of uncertainty (e.g. confidence intervals)
☒	☐	For null hypothesis testing, the test statistic (e.g. F, t, r) with confidence intervals, effect sizes, degrees of freedom and P value noted *Give P values as exact values whenever suitable.*
☒	☐	For Bayesian analysis, information on the choice of priors and Markov chain Monte Carlo settings
☒	☐	For hierarchical and complex designs, identification of the appropriate level for tests and full reporting of outcomes
☒	☐	Estimates of effect sizes (e.g. Cohen's d, Pearson's r), indicating how they were calculated

Our web collection on statistics for biologists contains articles on many of the points above.

Software and code

Policy information about availability of computer code

Data collection	Custom Python scripts were used to analyze Raman spectral mapping data by comparing peak intensity ratios and peak height. Graphene yield was calculated using I2D/IG ratios from these analyses. We looked for the I2D/IG > 0.3 then divided those ratios by the total number of spectra collected to give the graphene yield. These scripts are available at https://github.com/jlb48249/FJH_ML.
Data analysis	Custom Python scripts were used to analyze Raman spectral mapping data by comparing peak intensity ratios and peak height. Graphene yield was calculated using I2D/IG ratios from these analyses. We looked for the I2D/IG > 0.3 then divided those ratios by the total number of spectra collected to give the graphene yield. These scripts are available at https://github.com/jlb48249/FJH_ML.

For manuscripts utilizing custom algorithms or software that are central to the research but not yet described in published literature, software must be made available to editors and reviewers. We strongly encourage code deposition in a community repository (e.g. GitHub). See the Nature Portfolio guidelines for submitting code & software for further information.

Data

Policy information about availability of data

All manuscripts must include a data availability statement. This statement should provide the following information, where applicable:

- Accession codes, unique identifiers, or web links for publicly available datasets
- A description of any restrictions on data availability
- For clinical datasets or third party data, please ensure that the statement adheres to our policy

Supplementary datasets for Monte Carlo LCA and TEA calculations are uploaded to Dryad. https://doi.org/10.5061/dryad.cc2fqz6h3.

Research involving human participants, their data, or biological material

Policy information about studies with human participants or human data. See also policy information about sex, gender (identity/presentation), and sexual orientation and race, ethnicity and racism.

Reporting on sex and gender	no human participants
Reporting on race, ethnicity, or other socially relevant groupings	no human participants
Population characteristics	no human participants
Recruitment	no human participants
Ethics oversight	no human participants

Note that full information on the approval of the study protocol must also be provided in the manuscript.

Field-specific reporting

Please select the one below that is the best fit for your research. If you are not sure, read the appropriate sections before making your selection.

☐ Life sciences ☐ Behavioural & social sciences ☒ Ecological, evolutionary & environmental sciences

For a reference copy of the document with all sections, see nature.com/documents/nr-reporting-summary-flat.pdf

Ecological, evolutionary & environmental sciences study design

All studies must disclose on these points even when the disclosure is negative.

Study description	samples were made in the lab
Research sample	sample size described in appropriate sections
Sampling strategy	samples were made in the lab
Data collection	data was collected from the instrumental outputs
Timing and spatial scale	none taken into consideration
Data exclusions	none
Reproducibility	sample size described in the manuscript and/or SI
Randomization	none
Blinding	none

Did the study involve field work? ☐ Yes ☒ No

Reporting for specific materials, systems and methods

We require information from authors about some types of materials, experimental systems and methods used in many studies. Here, indicate whether each material, system or method listed is relevant to your study. If you are not sure if a list item applies to your research, read the appropriate section before selecting a response.

Materials & experimental systems

n/a	Involved in the study
☒	☐ Antibodies
☒	☐ Eukaryotic cell lines
☒	☐ Palaeontology and archaeology
☒	☐ Animals and other organisms
☒	☐ Clinical data
☒	☐ Dual use research of concern
☒	☐ Plants

Methods

n/a	Involved in the study
☒	☐ ChIP-seq
☒	☐ Flow cytometry
☒	☐ MRI-based neuroimaging

Plants

Seed stocks	plants were not used in this study
Novel plant genotypes	plants were not used in this study
Authentication	plants were not used in this study